remote sensing

MDPI

Article

Investigating Synoptic Influences on Tropospheric Volcanic Ash Dispersion from the 2015 Calbuco Eruption Using WRF-Chem Simulations and Satellite Data

Douglas Lima de Bem [1], Vagner Anabor [1], Franciano Scremin Puhales [1], Damaris Kirsch Pinheiro [1], Fabio Grasso [2], Luiz Angelo Steffenel [3], Leonardo Brenner [3] and Umberto Rizza [2,*]

[1] Department of Physics (UFSM), Federal University of Santa Maria, Santa Maria 97105-900, Brazil; douglas.lima@acad.ufsm.br (D.L.d.B.); vanabor@ufsm.br (V.A.); franciano.puhales@ufsm.br (F.S.P.); damaris@ufsm.br (D.K.P.)
[2] National Research Council—Institute of Atmospheric Sciences and Climate (CNR-ISAC), 73100 Lecce, Italy; fabiomassimo.grasso@cnr.it
[3] Laboratoire d'Informatique en Calcul Intensif et Image pour la Simulation (LICIIS), Université de Reims Champagne-Ardenne, 51100 Reims, France; luiz-angelo.steffenel@univ-reims.fr (L.A.S.); leonardo.brenner@univ-reims.fr (L.B.)
* Correspondence: umberto.rizza@cnr.it

Abstract: We used WRF-Chem to simulate ash transport from eruptions of Chile's Calbuco volcano on 22–23 April 2015. Massive ash and SO_2 ejections reached the upper troposphere, and particulates transported over South America were observed over Argentina, Uruguay, and Brazil via satellite and surface data. Numerical simulations with the coupled Weather Research and Forecasting–Chemistry (WRF-Chem) model from 22 to 27 April covered eruptions and particle propagation. Chemical and aerosol parameters utilized the GOCART (Goddard Chemistry Aerosol Radiation and Transport) model, while the meteorological conditions came from NCEP-FNL reanalysis. In WRF-Chem, we implemented a more efficient methodology to determine the Eruption Source Parameters (ESP). This permitted each simulation to consider a sequence of eruptions and a time varying ESP, such as the eruption height and mass and the SO_2 eruption rate. We used two simulations (GCTS1 and GCTS2) differing in the ash mass fraction in the finest bins (0–15.6 µm) by 2.4% and 16.5%, respectively, to assess model efficiency in representing plume intensity and propagation. Analysis of the active synoptic components revealed their impact on particle transport and the Andes' role as a natural barrier. We evaluated and compared the simulated Aerosol Optical Depth (AOD) with VIIRS Deep Blue Level 3 data and SO_2 data from Ozone Mapper and Profiler Suite (OMPS) Limb Profiler (LP), both of which are sensors onboard the Suomi National Polar Partnership (NPP) spacecraft. The model successfully reproduced ash and SO_2 transport, effectively representing influencing synoptic systems. Both simulations showed similar propagation patterns, with GCTS1 yielding better results when compared with AOD retrievals. These results indicate the necessity of specifying lower mass fraction in the finest bins. Comparison with VIIRS Brightness Temperature Difference data confirmed the model's efficiency in representing particle transport. Overestimation of SO_2 may stem from emission inputs. This study demonstrates the feasibility of our implementation of the WRF-Chem model to reproduce ash and SO_2 patterns after a multi-eruption event. This enables further studies into aerosol–radiation and aerosol–cloud interactions and atmospheric behavior following volcanic eruptions.

Keywords: WRF-Chem; Calbuco; ash; synoptics; aerosols

Citation: de Bem, D.L.; Anabor, V.; Puhales, F.S.; Pinheiro, D.K.; Grasso, F.; Steffenel, L.A.; Brenner, L.; Rizza, U. Investigating Synoptic Influences on Tropospheric Volcanic Ash Dispersion from the 2015 Calbuco Eruption Using WRF-Chem Simulations and Satellite Data. *Remote Sens.* **2024**, *16*, 4455. https://doi.org/10.3390/rs16234455

Academic Editor: Ciro Del Negro

Received: 2 October 2024
Revised: 20 November 2024
Accepted: 24 November 2024
Published: 27 November 2024

1. Introduction

Recent studies have shown the impact on the Earth's energy balance of ingesting aerosols from volcanic eruptions into the atmosphere [1,2], along with the impact of aerosols on cloud microphysics [3]. Volcanic explosions inject volcanic ash, sulfur-bearing

gases (mostly SO_2), water vapor, CO_2, halogens, N_2, and other species into the lower stratosphere [4]. According to Arghavani et al. [5] and Tsigaridis et al. [6], the annual emission of sulfur dioxide (SO_2) can reach 9.2 Tg year^{-1} between natural and anthropogenic production. Even though anthropogenic production is five times higher than volcanic emissions, its effects are weaker due to the higher efficiency of volcanic sulfur in producing sulfate aerosols, which can be up to 4.5 times higher. This occurs because volcanic SO_2 is emitted at high temperatures and reaches the stratosphere, where it has a longer residence time [5]. As examples of direct impacts from the absorption of solar radiation by these aerosols, the eruptions of Mount Pinatubo in 1991 resulted in global cooling of 0.5 °C in the following years [7], while the Hunga Tonga eruption in 2022 produced an exceptionally large quantity of stratospheric aerosol, directly impacting the radiative balance [8].

Calbuco can be considered a major volcano in South America, and its eruptions may have a considerable impact in the Andes area and countries bordering the Chilean territory [9]. Before 2015, eleven historical eruptions of Calbuco had been recorded since 1792, three of which had a Volcanic Explosivity Index (VEI; [10]) of order 3 or higher. The last major eruption in 1961 generated a volcanic plume approximately 12 km high and produced around 0.07 km^3 Dense Rock Equivalent (DRE) (about 0.2 km^3 bulk), impacting the northeast sector of the volcano, including the city of Bariloche in Argentina [11–13]. According to the report of the Chilean SERNAGEOMIN, during the month of April 2015 the volcano erupted again on the 22nd and 23rd, producing columns of debris and smoke that reached altitudes of 17 km. Initially, the debris spread northwest of the volcano, and in the following days it was carried across regions of Argentina, Uruguay, and Brazil.

The April 2015 Calbuco eruptions were investigated by Bègue et al. [14] utilizing satellite data and lidar observations that highlighted the "Calbuco aerosol signal" on the Indian Ocean at Reunion Island one week after the first eruption (22 April), while JS Lopes et al. [15] investigated the transport of volcanic ash in South America with a suite of remote sensing data, indicating that the Calbuco volcanic aerosol layers could be classified as sulfates with some ash type. Van Eaton et al. [16] identified a new approach to quantify eruptive processes by combining lightning and umbrella expansion rates from the 2015 Calbuco eruption, and suggested that ice formation above 10 km controlled the propagation of volcanic lightning downwind. For the same eruption, Romero et al. [17] presented a study using ground and satellite data to analyze the propagation of tephra (particulate material produced from a volcanic eruption) across the region near the event. Marzano et al. [18] used various ground and satellite sensors to conduct a study on the propagation of volcanic ash and plumes, employing MODIS, VIIRS, and CALIOP sensors, among others, along with a thorough investigation of particle size. They were able to demonstrate that the propagation of particulates occurred at higher atmospheric levels between 15 and 20 km.

Numerical simulations of volcanic plumes have attracted increasing attention from the geophysics research community because of the deep impact of volcanic emissions on aviation and ground structures. Despite the understanding gained from remote sensing measurements, the numerical modeling of volcanic eruptions still remains an important scientific challenge. Several studies have aimed to represent the Calbuco 2015 eruption through the use of numerical modeling, such as Mastin and Van Eaton [19], who employed the Ash3d model, and [20], who considered an umbrella cloud model based on the calculation of downwind advection, turbulent diffusion, and particle settling. Such studies are of great importance for understanding the dynamics of the plume originating from the eruption, and have already been conducted for events such as the Pinatubo (1991) and Kelud (2014) eruptions. However, these simulations fall short in representing the atmospheric processes and their active role in transporting particulates across the region. Eruption source parameters such as the plume height, Mass Eruption Rate (MER), and onset and end times of the paroxysm need to be specified in a realistic way in order to obtain the forecast of ash column loading distributions for mapping flight hazard areas at the free troposphere levels [21]. The WRF–Chem model has been previously applied to study the

transport of ash and SO_2 from volcanic eruptions all over the world. Stuefer et al. [22] made important progress on the WRF-Chem architecture, implementing specialized routines allowing for simulation of the emission, transport, and settling of volcanic particles and gases. Stenchikov et al. [23] recently applied the WRF-Chem model to study the radiative impact on the stratosphere caused by the Hunga eruption on 15 January 2022. They presented a sophisticated approach using the sectional Model for Simulating Aerosol Interactions (MOSAIC; [24]). MOSAIC explicitly accounts for cloud–aerosol interactions, including aqueous chemistry and aerosol wet removal [25].

The higher-latitude regions of South America are directly impacted by the passage of meteorological systems known as transient systems [26]. These systems function to transport air masses between the tropics and mid-latitudes. Marengo and Seluchi [27] indicated the orographic influence of the Andes Mountains on synoptic systems, which act as a barrier to zonal flow in the Southern Hemisphere, finding that the greatest influence is between 10° and 40°S. In this range, the westerly flow is completely blocked in the lower troposphere, channeling the meridional flow. Several studies have indicated that this orographic influence favors the rapid northeastward propagation of transient systems crossing the Andes [28,29]. Satyamurty et al. [30] used a numerical model to analyze the influence of the Andes, showing that the orography favors the intensification of lee cyclogenesis on the leeward side of the mountains. These are so-called due to their movement along the region, and their analysis is fundamental when discussing the transport of aerosols throughout the troposphere. The current literature has gaps in the analysis of particulate transport during the event in question, specifically regarding which meteorological systems were most crucial in carrying volcanic ash from a volcano in southern Chile to regions of Argentina and Brazil.

In this study, we make use of the WRF-Chem model to describe the two eruptions of the Calbuco volcano that occurred on 22 and 23 April 2015. From the meteorological perspective, we analyze the transport of tropospheric volcanic ash in South America and its relationship with the synoptic system. From a general point of view, the impact of the Calbuco eruption has been largely documented by different techniques and different authors; however, few studies have used this event to test the WRF-Chem model under the volcanic configuration, and this approach is important for studies that require an integrated approach between meteorology and aerosols and their mutual feedback.

To perform a comprehensive validation, we first analyzed the synoptic patterns during and after the eruptions by analyzing the satellite products of the VIIRS sensor in the visible (AOD) and thermal IR (BTD) channels, then compared the simulated data with AERDB_D3_VIIRS_SNPP data and with the SO_2 concentration from the OMPS (Ozone Mapping and Profiler Suite) sensor onboard the SUOMI-NPP spacecraft.

2. Materials and Methods

2.1. Description of the Event

Detailed descriptions of the 22–23 April (2015) eruption of Calbuco in Chile have been reported by Romero et al. [17], Van Eaton et al. [16], and Marzano et al. [18], among others. The first eruption started at 21:05 (UTC) on 22 April; the ash column rose to 16 km and ejected approximately 40 million cubic meters of ash in about 90 min [16,17]. The second eruption began at 04:00 UTC on 23 April, with an ash column reaching 17 km, and ejected around 170 million cubic meters of ash over 6 h (see Table 1 (https://rnvv.sernageomin.cl/, https://volcanicdegassing.wordpress.com/2015/04/27/volcan-calbuco-what-do-we-know-so-far/; accessed on 21 September 2022) [16,17]. The magma involved in the eruption was a typical Eruption Source Parameters (ESP) S-type eruption with andesite/dacite, containing volcanic glass and crystals of plagioclase and amphibole along with minor quartz and biotite [17]. The SO_2 gas release from the eruption was substantial at around 0.2–0.4 million tons, but probably some way short of the levels needed to have a significant impact on the climate system [14,31].

Table 1. Eruption parameters (SERNAGEOMIN).

Start Time UTC	Durantion min	Emiss Height km	Emiss Ash Rate kg s^{-1}	Emiss SO_2 kg h^{-1}
22 April 2015—21:00	90	16	0.740×10^7	0.133×10^9
23 April 2015—04:00	360	17	0.787×10^7	0.4×10^8

2.2. Synoptic Analysis During the Event

Usually, synoptic systems evolve over a timescale of a couple of days, making time frames between 12–24 h sufficient to represent the evolution of atmospheric processes at this timescale. On 22 April, before the eruption, a stable atmospheric pattern was observed in a synoptic environment influenced by a high-pressure system, calm winds, and a thermodynamic profile with a strong temperature inversion at the top of the planetary boundary layer (PBL). This is a typical profile of inversion due large-scale subsidence, and can be observed in Figure A6. The first Calbuco eruption started at 21:00 UTC on 22 April 2015; a few hours later, at 00:00 UTC on 23 April 2015, a transient elongated anticyclonic high-pressure system (High) was located over the Pacific Ocean along the Southern Chilean coastal range at low levels, between latitudes 30°S and 45°S (Figure 1c). This high ridge (indicated in Figures 1c, 2c, 3c and 4c by the symbol of the black zigzag line) extended over the eruption area in a thermally homogeneous and weak pressure gradient environment, creating a statically stable and low wind shear environment in the lower troposphere. This scenario provided the dynamic and thermodynamic conditions for the Calbuco eruption plume to rise vertically and rapidly reach the stratosphere. The geopotential height field at 500 hPa shows a long wave pattern extending from the Pacific to the Atlantic Ocean below 40°S (Figure 1d) just south of the eruption area, with the geostrophic flow mainly westward, accelerating the erupted mass portion across the Andes towards Argentina at this level. In the middle troposphere, a Cut-Off Low (COL) pressure system was forming ahead and detaching from a mid-latitude shortwave in the westerlies that was amplifying from the Buenos Aires region towards the Pacific Ocean (30°S, 90°W) [32,33]. This COL system would play an important role in the following hours by trapping a portion of particulate material and gases from the eruption on the west side of the Andes. At upper levels of the troposphere, the eruption area was upstream of a long wave trough in which the polar upper-level jet was embedded (Figure 1b). An amplifying shortwave was located over the COL, as observed in the 200 hPa wind field. South of the eruption area, a diffluent flow split from the polar jet towards the subtropical jet entrance region, forming a northward flow on the lee side of the Andes (Figure 1b). This caused the first volcanic plume to be advected and spread northward. The position between the subtropical and polar upper-level jets was still far from their vertical motion influence perimeters, being in a favorable to neutral region for vertical motions relative to the 200 hPa wind field [34,35]. At levels close to the surface, the influence of the high-pressure system in the Pacific could be observed, with its anticyclonic circulation helping the winds transport the plume towards the northwest, possibly crossing the Andes Mountains (Figure 1a,c). During the next day after the first eruption, synoptic conditions favored a higher concentration of the plume in the region near the volcano, with upward movement promoting the vertical propagation of this plume. At lower levels, circulation favored transport towards the Pacific, while at higher levels stability favored the concentration of the plume over the region.

In the first hours of 24 April 2015, the low-level atmospheric features presented almost the same conditions, keeping the conditions favorable for the thermal volcanic plume to ascend vertically in a low wind shear environment (Figure 2a). The sea-level pressure field corroborates the previously indicated information (Figure 1c), with a high-pressure system acting over the regions of Argentina, Uruguay, and Brazil. However, the geopotential horizontal gradient is stronger at 500 hPa, denoting an intensification of the eastward geostrophic advection by geostrophic wind at this level (Figure 2d). The 500 hPa amplified

shortwave formed a COL upstream in the Andes and a high-level cyclonic vortex (HCV) over South Brazil, with both systems acting as convergence centers. The COL kept a small portion of the plume east of the Andes, and the HCV pulled the plume to low latitudes. The polar upper-level jet streak at 200 hPa was displaced eastward (Figure 2b); by this time, the Calbuco area was at the equatorial entrance (superior area) of the polar upper-level jet streak, a favorable region for upward vertical motion [35]. The subtropical jet stream also moved eastward over South Brazil, acting as a kinetic barrier preventing the plume from reaching São Paulo, the most populated city and most important commercial aviation center in South America. The mean upper-level flow between the jet streaks drove the plume east equatorward along a SW–NE orientation (Figure 2b). During the second day of the event, the transport of particulates at both the lower and upper levels of the troposphere was directed over the regions of Argentina, Uruguay, and Brazil as a direct result of the influence of synoptic systems.

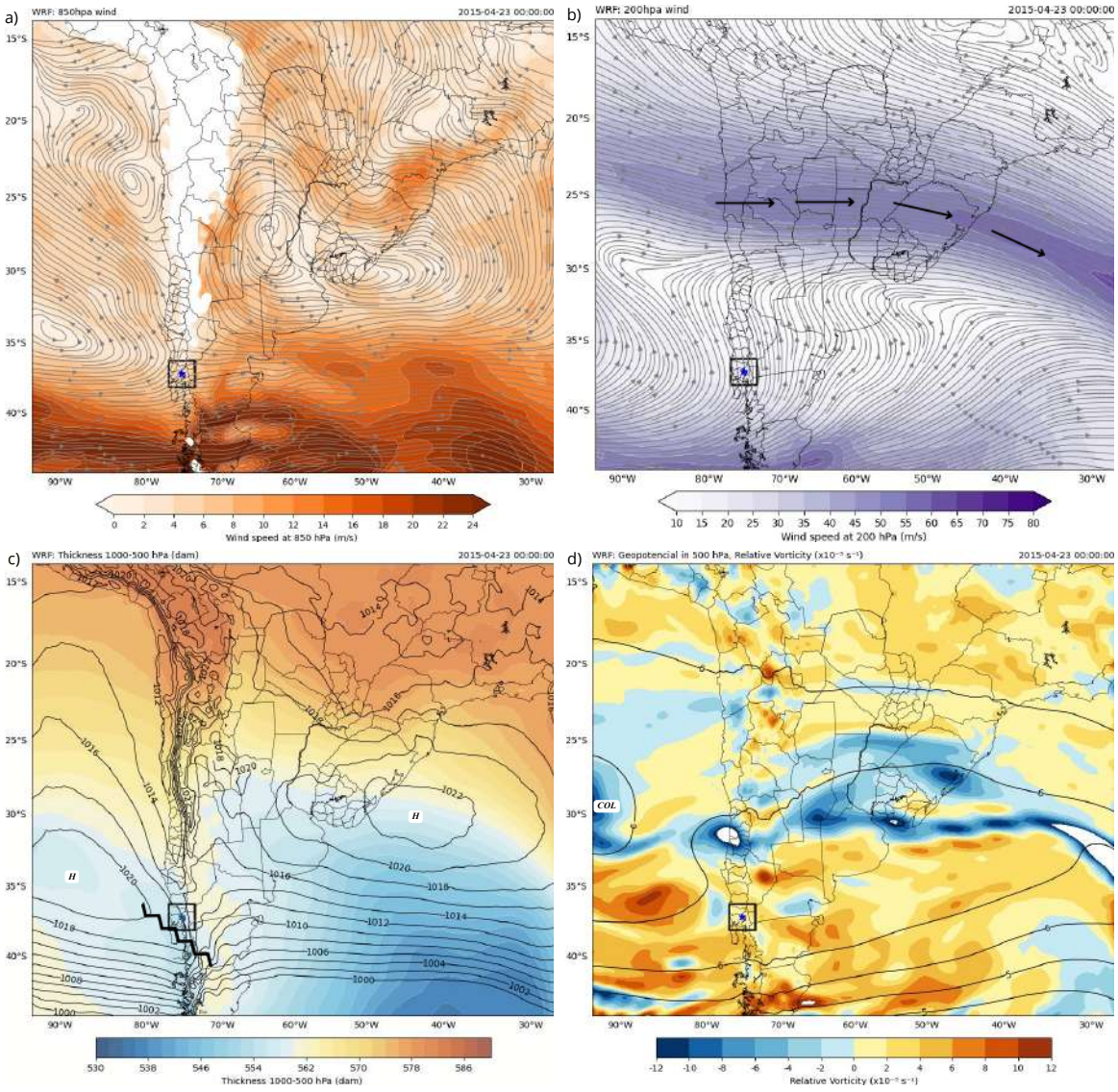

Figure 1. Synoptic fields on 23 April at 00:00 UTC from the WRF model: (**a**) wind field at 850 hPa; (**b**) wind field up to 200 hPa (the solid arrows indicate the subtropical jet); (**c**) surface pressure (isolines) and thickness 500−1000 hPa field (shaded contours); (**d**) geopotential at 500 hPa (isolines) and relative vorticity field (shaded contours). The blue dot indicates the location of the Calbuco volcano.

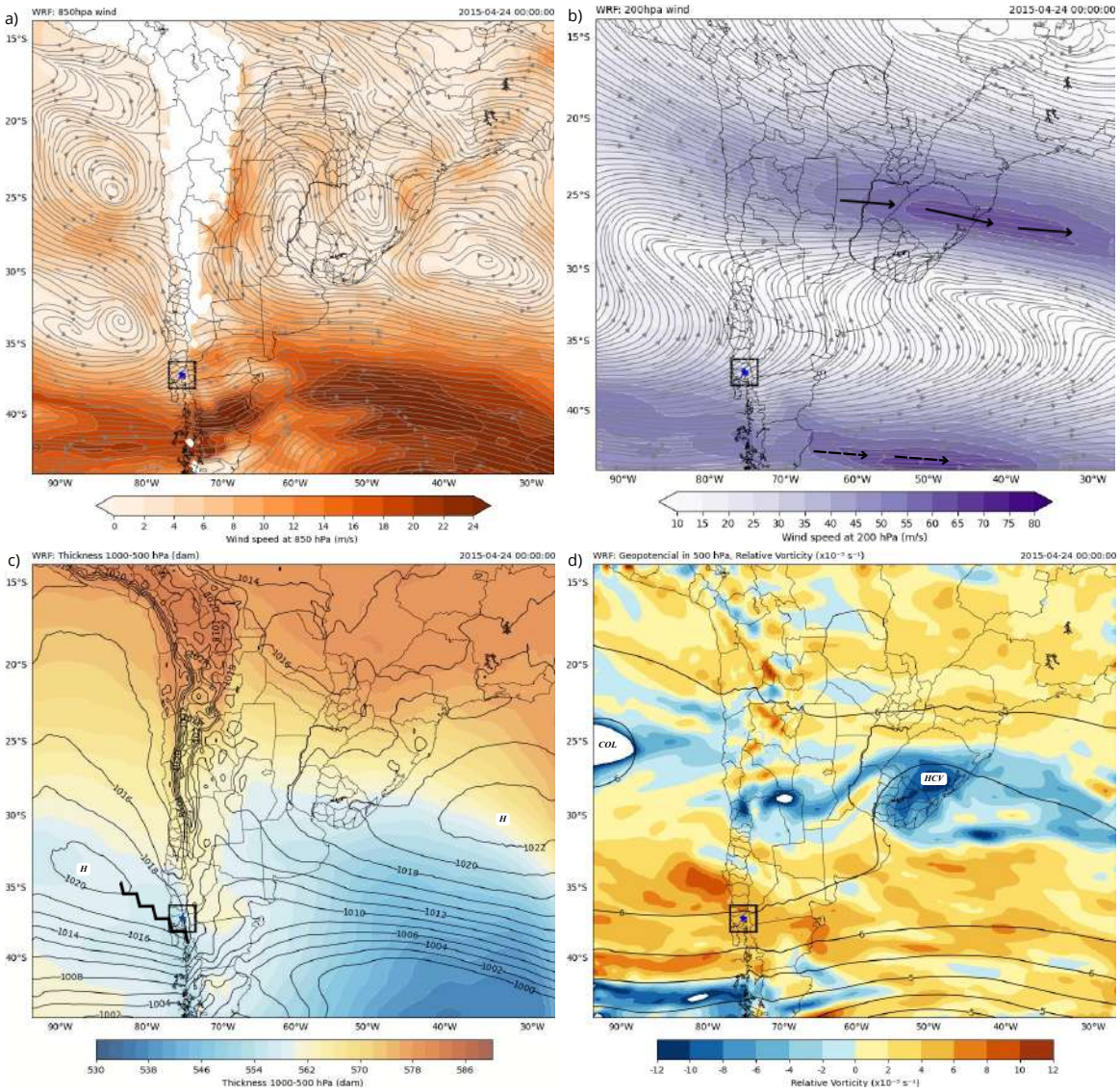

Figure 2. Synoptic fields on 24 April at 00:00 UTC from the WRF model: (**a**) wind field at 850 hPa; (**b**) wind field up to 200 hPa (the solid arrows indicate the subtropical jet and the dashed arrows indicate the polar jet); (**c**) surface pressure (isolines) and thickness 500−1000 hPa field (shaded contours); (**d**) geopotential at 500 hPa (isolines) and relative vorticity field (shaded contours). The blue dot indicates the location of the Calbuco volcano.

Two days after the last volcanic eruption, on 25 April 2015, areas with high concentrations of volcanic gases and aerosol particles [16,31,36] were still present in the upper troposphere. Weak thickness and pressure gradients at mid-latitudes all over South America indicated low wind speed and a thermally homogeneous environment (Figure 3a,c); at this moment, the volcanic plume was mostly concentrated at the high levels of the troposphere. At 500 hPa, it can be seen that the COL and HCV systems have intensified and are deeper than the previous day, while a cyclonic vorticity channel (indicated by the blue colors of relative vorticity) connects the two systems (Figure 3d). The upper flow at 200 hPa (Figure 3b) presents a short ridge over southern Argentina and a short trough over southern Brazil, and denotes the high influence of the upper-level flow spreading the volcanic plume. The subtropical jet stream entrance region is over Southern Brazil, and the 200 hPa streamlines present a high confluence in the region that increases the local plume concentration (Figure 3b). The propagation of the wave seen in the geopotential and relative vorticity fields (Figure 3d) allows for transport of the plume in the upper

troposphere to regions of lower latitudes, potentially reaching southeastern Brazil. By the end of the third day of the event, the plume's propagation in the upper troposphere can be observed reaching the southeastern region of Brazil. Meanwhile, due to the stability generated by the high-pressure system and its circulation, the highest concentration of the plume at lower levels remains around the region between the three countries on 24 April.

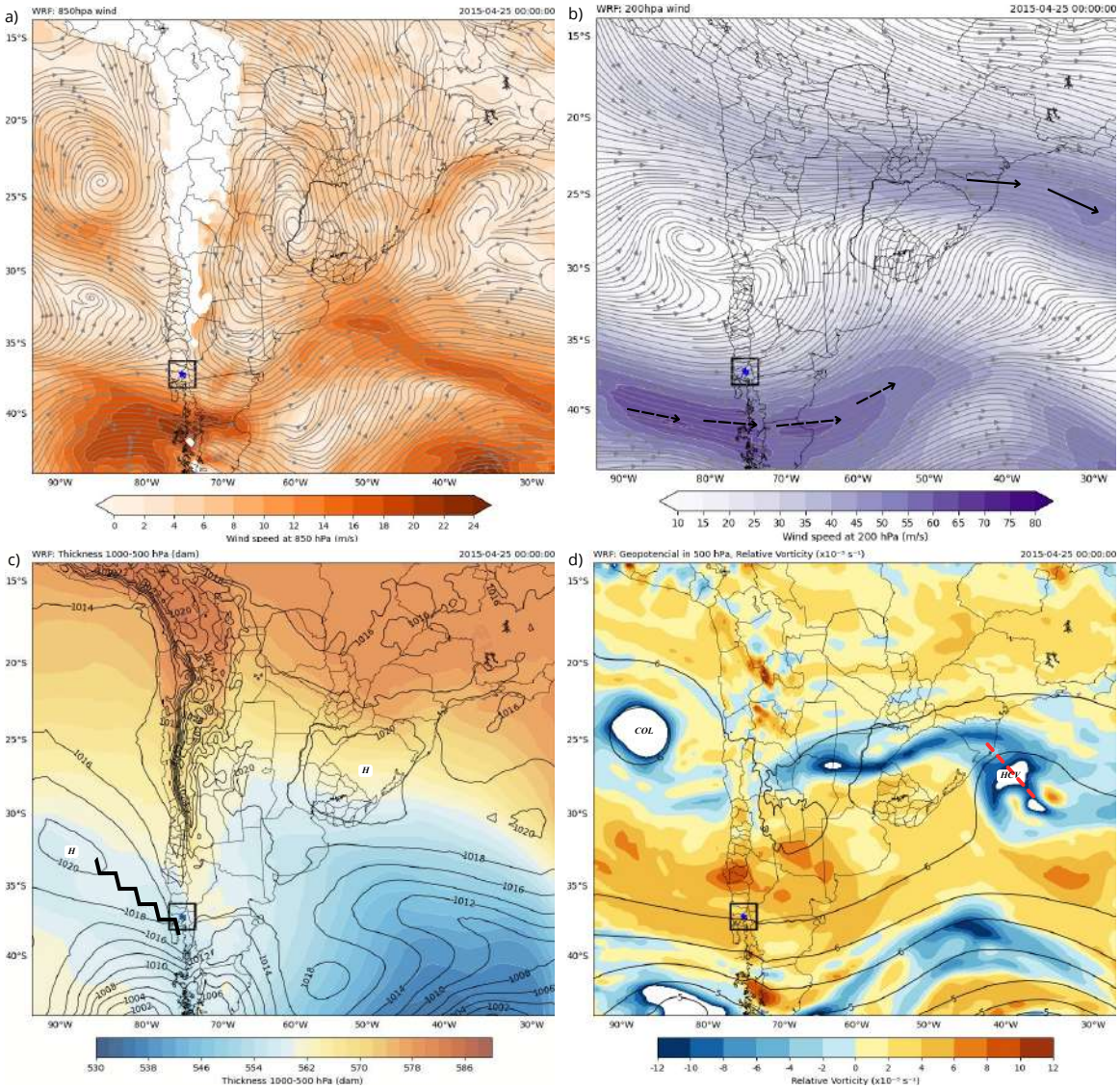

Figure 3. Synoptic fields on 25 April at 00:00 UTC from the WRF model: (**a**) wind field at 850 hPa; (**b**) wind field up to 200 hPa (the solid arrows indicate the subtropical jet and the dashed arrows indicate the polar jet); (**c**) surface pressure (isolines) and thickness 500−1000 hPa field (shaded contours); (**d**) geopotential at 500 hPa (isolines) and relative vorticity field (shaded contours). The red dashed line indicates the trough axis, while the blue dot indicates the location of the Calbuco volcano.

On 26 April 2015, the upper-level systems evolved eastward, while the high-confluence area at the entrance of the subtropical jet was displaced over São Paulo and advected the plume over the city (Figure 4b). The active trough moving over the region also played an important role in the transport of the plume at upper levels (Figure 4d). As the local and synoptic effects diminished in influence over the days following the eruption, the plume was transported as indicated above to the southeast region of Brazil, thereby reducing its concentration over the event area. During this eruption, the subtropical jet stream and polar jet stream acted as kinetic barriers to the plume's advection, with the momentum transference between them determining the advection [29,35]. At lower levels, the movement of

the high-pressure system located over the southern region of Brazil (Figure 4c) favored the transport of the plume over the region throughout the day due to its circulation (Figure 4a), resulting in greater dispersion compared to the previous day. During the period following the volcanic eruption, direct impact of synoptic conditions on plume transport over the region can be observed [26,28]. At lower levels, the high-pressure systems initially favored transport towards the Pacific on the first day; subsequently, the formation of another high-pressure system over the region between Argentina and Brazil favored transport towards lower latitudes. At upper levels, it can be seen that the vertical development was more intense due to an initial southwesterly circulation at 200 hPa, helping the plume to reach higher altitudes and even into the stratosphere [18]. With the movement of the trough on April 24 and 25, this plume, which had previously reached the upper levels, was transported over the southern regions of Brazil, Uruguay, and central Argentina. Through the development of all these synoptic systems, the plume was eventually transported over the entire region.

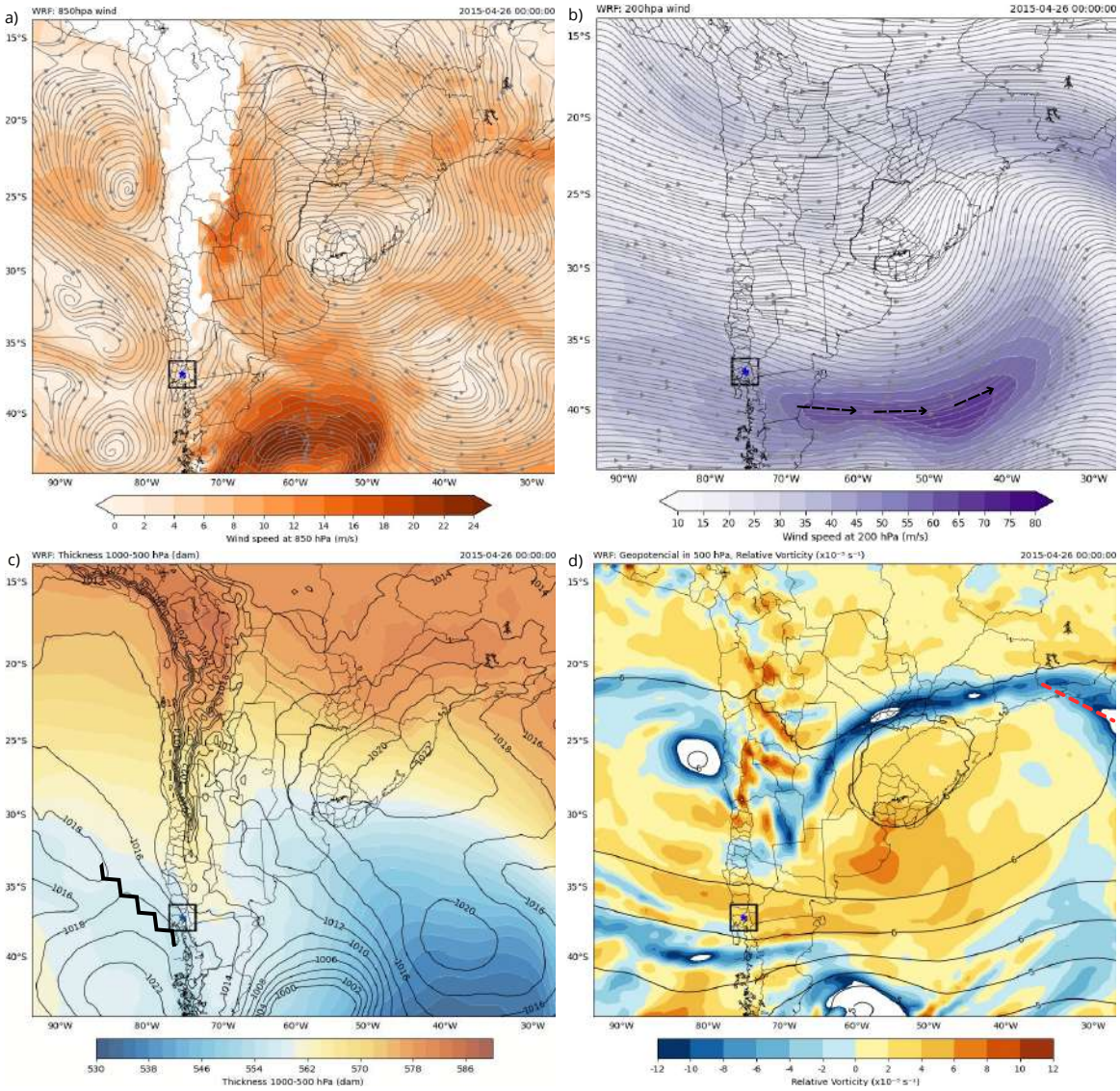

Figure 4. Synoptic fields on 26 April at 00:00 UTC from the WRF model: (**a**) wind field at 850 hPa; (**b**) wind field up to 200 hPa (the solid arrows indicate the subtropical jet and the dashed arrows indicate the polar jet); (**c**) surface pressure (isolines) and thickness 500−1000 hPa field (shaded contours); (**d**) geopotential at 500 hPa (isolines) and relative vorticity field (shaded contours). The red dashed line indicates the trough axis, while the blue dot indicates the location of the Calbuco volcano.

2.3. Orography Influence

The Andes Cordillera, the largest and tallest mountain range in the Southern Hemisphere, runs continuously along the Pacific coast of South America, having a direct impact on the passage of meteorological systems and synoptic fields. For studies on the transport of aerosol particulates, it is of utmost importance to understand the wind field alongside topographic analysis. Such topographic analysis indicates that circulations associated with topography are crucial for defining air trajectories, which are necessary for assessing the impact of atmospheric pollution. Additionally, it is known that regions with complex topography can have direct impacts on large-scale movements [37]. Another study by Seluchi et al. [29] highlights the blocking effect generated by the mountain range along the zonal flow at lower levels. Due to its height, the mountain range acts to prevent the spread of easterly winds, thereby intensifying upward movement, which impacts not only the zonal flow but also the thermal field over the South American region. Based on the analysis of data observed during the volcanic eruption, the mountain range acted as a barrier to the eastward transport of ash particles while also favoring orographic upward flow, suggesting propagation along the stratosphere.

2.4. WRF-Chem Model: Setup for Volcanic Emissions

A new functionality in the Weather Research and Forecasting (WRF) with Chemistry (WRF-Chem, [38]) model has recently been included to allow for simulation of the emission, transport, transformation, and settling of aerosols and gases released during volcanic eruptions [22]. Many specialized options are available for the treatment of volcanic ashes and gas (SO_2); among the most common, we mention (i) the invariant tracer using four ash variables and no chemistry modules (`chem_opt = 401`), (ii) the intermediate options using ten ash variables and SO_2 (`chem_opt = 402`), and (iii) a more sophisticated approach that utilizes the GOCART-SIMPLE option (`chem_opt = 300`) with all optical drivers activated [39]. As reported in Table 1, the ESPs define the plume altitude, the mass of the eruption cloud, and the particle size distributions. It is important to mention that Mastin et al. [40] have developed ESPs for all of the world's volcanoes along with their "typical" eruption profiles. In this context, all possible eruption categories can be classified into either M-type (mafic), which include basaltic and ultramafic magmas, or S-type (silicic), which include andesite, dacite, and rhyolite, and others such as phonolite that can produce high ash columns ([40]).

Table 2 provides the selected particle size bins associated with the WRF-Chem variable names `vash_1` to `vash_10` and the corresponding mass fraction percentage for each S-type volcano distribution. The mass fraction was configured by Steensen et al. [41] and Stuefer et al. [22] considering previous works from Scollo et al. [42] and Rose and Durant [43], among others. To select the appropriate ESP during a specific volcanic eruption event, it is possible to use the emission preprocessing package PREP_CHEM_SRC [44], which incorporates the full database developed by Mastin et al. [40] (M09). This provides information on 1535 volcanoes around the world, comprising their location (latitude, longitude, and height) as well as the corresponding historical ESP [22]. The default configuration for Calbuco considers an ESP of type S2, with (lat, lon) coordinates and an elevation of 2003 m. Moreover, preprocessing provides the proper localization of the selected volcano in the domain grid, as reported in Figure 5.

Table 2. Ash particle bin size ranges with corresponding WRF-Chem variable names; the mass fractions in percent of the total mass are provided for each ESP type-S.

Var	Size Bins	S0	S1	S2	S3	S8	S9
vash_8	7.8125–15.625 µm	8.0	1.3	8.0	15.0	15.0	18.0
vash_9	3.9065–7.8125 µm	5.0	0.6	5.0	10.0	10.0	7.0
vash_10	<3.9065 µm	3.0	0.5	3.5	11.2	11.2	0.0

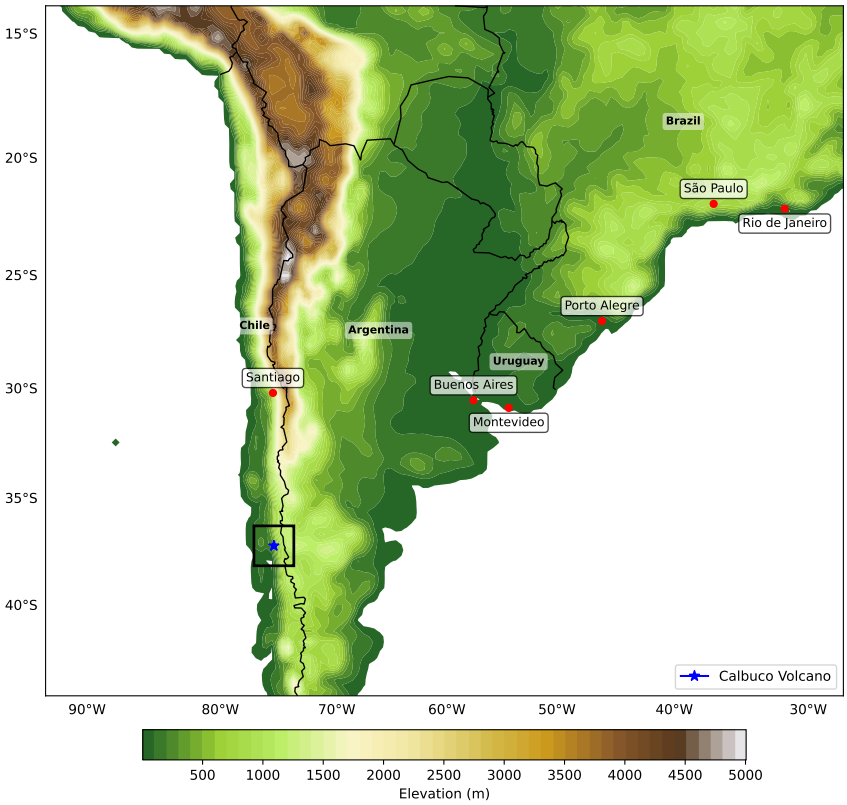

Figure 5. Domain numerical grid showing the model representation of elevation and the location of Calbuco (blue star) along with the main cities in South America (red points).

The numerical grid has (150, 130) grid points with `geog_data_res = '30s'` and (dx, dy) = (30, 30) km upon a polar map projection. The dominant meteorological pattern is established based on the characteristics of the wind field, and consequently on the meso- and synoptic-scale pressure gradients. Additionally, it depends on the characteristics of the thermodynamic vertical profile, specifically, the temperature profile. Patterns with these characteristics are well represented at scales of 25 to 30 km. Higher-resolution simulations model sub-kilometric processes or even turbulent scales with physical forcings that are orders of magnitude smaller than those represented here. The simulation started at "2015-04-22_00:00:00" and stopped at "2015-04-27_00:00:00". The Initial Conditions (ICs) and Boundary Conditions (BCs) were provided by the NCEP-FNL (Final) operational global analysis/forecast fields at 0.25° spatial resolution [45]. In WRF-Chem, the emissions units for volcanic ash rate (`E_VASH`) are µg m^{-2} s^{-1} and the units for SO_2 (`E_VSO2`) are mol h^{-1} km^{-2}. In Table 1, the total erupted mass is calculated using the corresponding erupted volume times the ash mass density, which is defined as being 2500 kg m^{-3}. The total emission ash rate is then distributed following a typical "umbrella" plume model [46] between ten bins of aerosol particles with the diameter size ranges reported in Table 2 [22]. Following the literature about this eruption, the height of the plume indicates a height above 15 km [47,48]. Note that the default ESP parameters for a given volcano/eruption may be overwritten in the WRF-Chem emission driver Fortran routine. This was done by manually changing the specialized subroutine for the volcanic emission; in our version of the WRF-Chem code, a multi-eruption scenario for a single run is allowed, as in the current case (see Table 1). Regarding the model setting of the physical parameters, the surface layer module corresponds to the Mellor–Yamada–Nakanishi–Niino (MYNN) [49,50] scheme (`sf_sfclay_physics = 5`), the RUC (Rapid Update Cycle) Land Surface Model [51] is used to represent the land surface interactions (`sf_surface_physics = 3`), and the MYNN 2.5 level [52] turbulent kinetic energy parameterization is used to describe the PBL parameterization (`bl_pbl_physics = 5`). Short- and long-wave radiation effects are modeled using the rapid radiative transfer model for both short- and

long-wave (`ra_sw_physics = ra_lw_physics = 4`), while the two-moment cloud model microphysics scheme of Morrison et al. [53,54] is used for the treatment of the microphysical processes (`mp_physics = 10`). The chemistry/aerosol setting is depicted in Table 3; the use of `chem_opt = 300`, that is, the GOCART aerosol model, activates the WRF-Chem optical modules. Aerosol optical properties are derived using the Maxwell–Garnett volume averaging mixing rule (`aer_op_opt = 1`), which allows for calculation of the extinction coefficients, from which the AOD can then be calculated. For this aerosol option, the finest three ash bins (`vash_8`, `vash_9`, and `vash_10`) are combined into a "p10" variable, which is generically defined as unspeciated aerosols in the WRF-Chem registry configuration. This option also allows for of consideration of the feedback between volcanic ash and the radiation and microphysics [22]. Two simulations were considered: the first, GCTS2, utilized the ash granulometry expressed by the S2 distribution reported in Table 2, while the second, GCTS1, was configured with the S1 ash distribution. The difference between these two distributions, show in the table 3, is the percent of mass fraction in `vash_8`–`vash_10`, which is 2.4% for S1 and 16% for S2. Under this condition, the GCTS1 simulation has a lower content of the finest ash.

Table 3. Volcanic setup of the WRF-Chem model.

Case	Chem_opt	Distribution	Vash_#	% Total Mass
GCTS2	300	S2	8–10	16.5
GCTS1	300	S1	8–10	2.4

2.5. Description of the Event by AOD from AERDB OMPS-SNPP

The Level-3 (L3) Deep Blue [55] daily aerosol products from the Suomi National Polar-orbiting Partnership (SNPP) spacecraft provide satellite-derived measurements of Aerosol Optical Depth (AOD) and their properties over land and ocean as daily gridded aggregates. The Deep Blue algorithm was initially developed to fill gaps in Aerosol Optical Depth (AOD) retrievals over bright surfaces such as deserts and urban areas, where existing 'Dark Target' (DT) [56] approaches based on dense dark vegetation assumptions fail. Since 2012, it has been complemented with the Satellite Ocean Aerosol Retrieval (SOAR; [57]) algorithm to provide aerosol data coverage over the ocean. Later, a second-generation approach was developed [55] to extend Deep Blue's coverage to darker surfaces. In principle, AERDB/AOD provides coverage for all snow-free and cloud-free land surfaces. This daily aggregated product (short name: AERDB_D3_VIIRS_SNPP (https://ladsweb.modaps.eosdis.nasa.gov/missions-and-measurements/products/AERDB_D3_VIIRS_SNPP, accessed on 15 July 2024)) utilized in this study is derived from the Version-2.0 (V2.0) L2 6-min swath-based products (AERDB_L2_VIIRS_SNPP), and is provided in a $1° \times 1°$ degree horizontal resolution grid. This Level 3 daily product (in netCDF format) contains 45 Science Data Set (SDS) layers that include the "Aerosol optical thickness estimated at 550 nm over land and ocean." It is represented in Figure 6, which reports the daily average AOD from AERDB (SNPP-D3-VIIRS) for (a) 23 April, (b) 24 April, (c) 25 April, and (d) 26 April. It can be observed from this AOD product that on 23 April there were high AOD values (greater than 1.5) in a region at around 300 km from the volcano (Figure 6a), indicating the absence of an efficient atmospheric transportation system of these ash particulates. This is presented in Figure 1a,c, where the high-pressure system and its anticyclonic circulation at low levels promote weaker transportation due to winds towards the northwest region and the Pacific. The statically stable environment and low wind shear in the lower troposphere favors uplift over the region, leading to a higher concentration of ash particulates on 23 April with low dispersion during the day. On the following day, the ash plume is further transported northeast towards Buenos Aires and southern Uruguay (Figure 6b) due to the displacement of the upper-level trough (Figure 2d). On 25 April, the conditions at low levels are similar to those of the previous days; however, the upper levels of the atmosphere are crucial for the dispersion of particles toward the regions of Argentina and Brazil (Figure 6c). This is due

to the horizontal geopotential gradient at 500 hPa in Figure 3d, which favors geostrophic advection in the eastward direction. The cyclonic vortex at high levels and the COL act as centers of convergence that facilitate the transport, aiding the displacement of the plume to lower latitudes. At 850 hPa, the anticyclonic circulation acting over the region of Argentina throughout the day on 24 April favors displacement of the plume towards the region of Uruguay, as seen in Figure 3a. On 25–26 April (Figure 6c,d), the plume is directed into the Atlantic along the coastline of southern Brazil. The upper-level systems evolve eastward, and the area of high confluence at the entrance of the subtropical jet is displaced over São Paulo, advecting the plume over the city. As seen in the synoptic analysis, the subtropical and polar jet streams played a fundamental role in the concentration and transport of the eruption plume due to their function as a kinematic barrier for the advection of the plume and the momentum transfer between them [29,35].

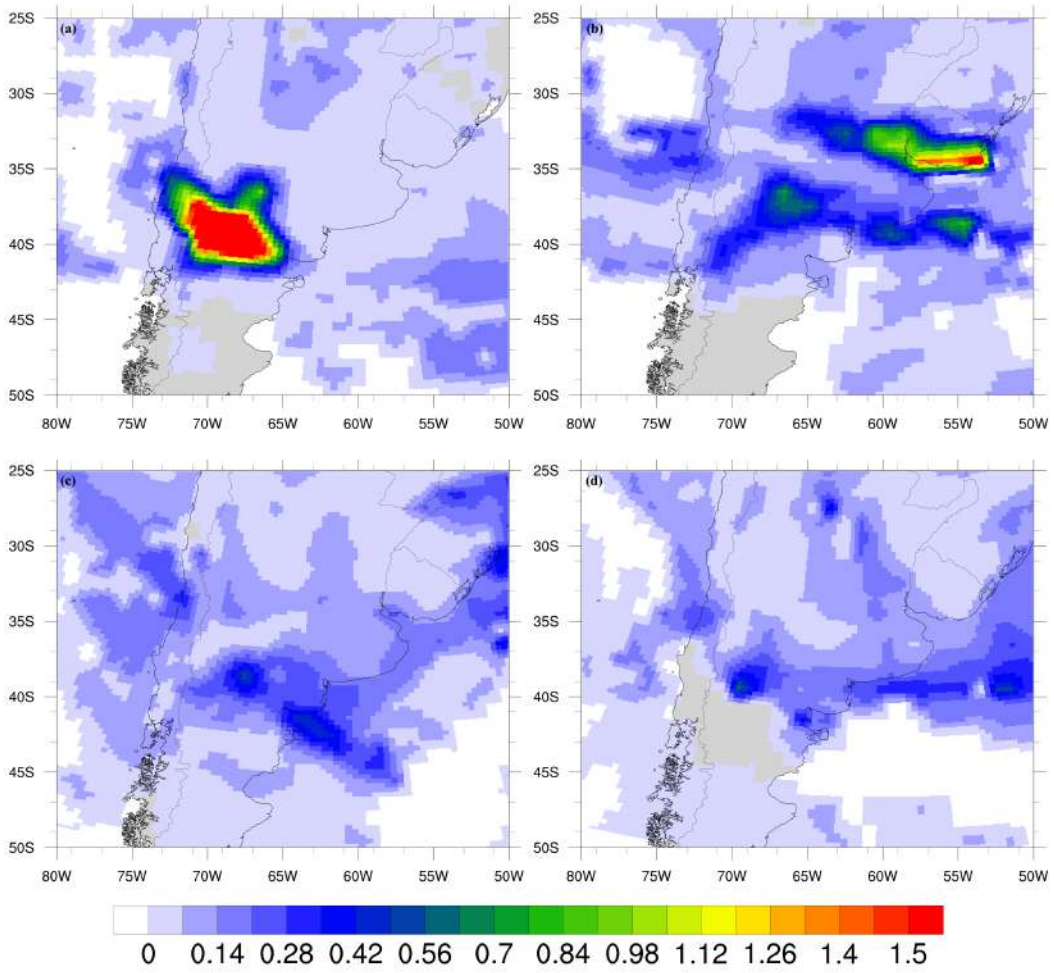

Figure 6. Daily average AOD from AERDB (SNPP-D3-VIIRS): (**a**) 23 April, (**b**) 24 April, (**c**) 25 April, and (**d**) 26 April.

2.6. Description of the Event by Split Windows Imagery from VIIRS

The use of the Brightness Temperature Difference (BTD) of the thermal infrared channels to track volcanic ash can be dated to Prata [58]. It is based on the reverse absorption effect (in the infrared window) observed for volcanic debris, which provides a signature that can be utilized to discriminate volcanic clouds from water/ice clouds [58]. Figure 7 shows the BTD of the VIIRS thermal infrared M-channels (700 m spatial resolution) calculated

following the split window volcanic ash detection method, which consists of calculating the difference between channels M15 (10.763 µm) and M16 (12.013 µm) of the VIIRS sensor:

$$BTD = BT_{15} - BT_{16}. \quad (1)$$

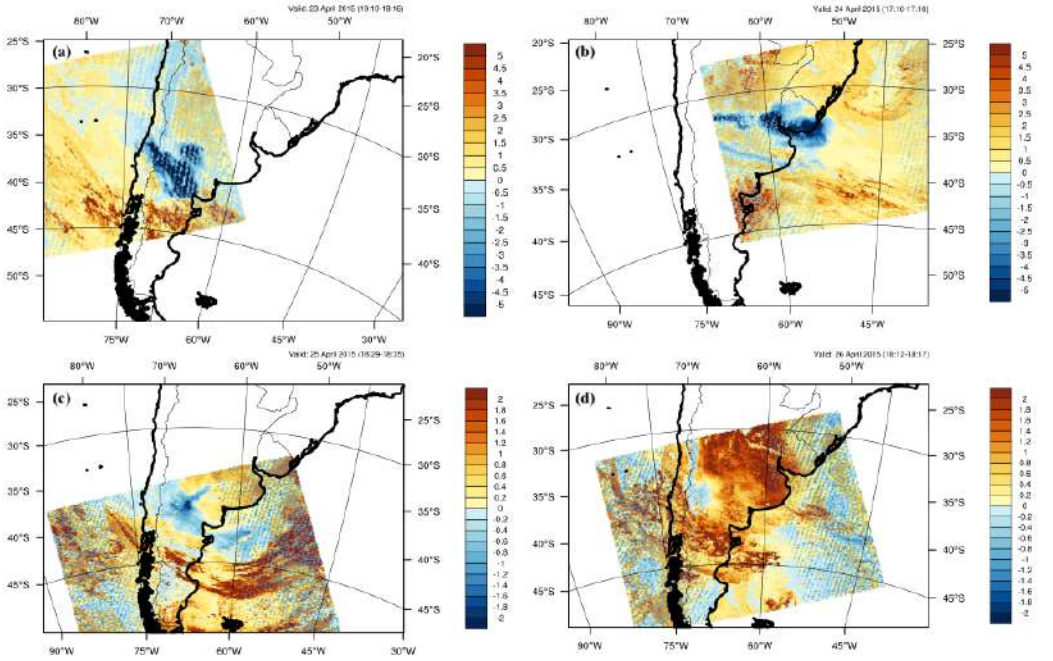

Figure 7. Brightness Temperature Difference (BTD) along the southern region of South America for (**a**) 23 April; (**b**) 24 April; (**c**) 25 April and (**d**) 26 April. Units are °K.

As depicted in Table 4, the SUOMI spacecraft had useful orbits in South America for the selected days, making it possible to draw the BTD map that is shown in Figure 7. The blue shaded regions in Figure 7 highlight the presence of ash plumes with BTD < 0; on the contrary, ice and water droplet clouds (yellow-red shaded) are denoted by regions with BTD > 0.

Table 4. Time granules of the SUOMI-NPP spacecraft over South America for 23–26 April 2015.

Day	Granule Time
23	19:10–19:16
24	17:10–17:16
25	18:29–18:36
26	18:12–18:17

Qualitative agreement is found with the AOD maps reported in Figure 6. Starting from 23 April (Figure 7a) until 26 April (Figure 7d), the position of the ash cloud in the four panels of Figure 7 is denoted by the region of blue shading, confirming transport of the ash plume as described above with regard to the synoptic pattern. Together with the analysis of AOD at 0.55 µm, this analysis based on IR channels provides a definitive picture of ash transport in South America after the 22–23 April 2015 Calbuco eruptions.

3. Results and Discussion

3.1. Comparison with Satellite Data

3.1.1. AERDB_D3_VIIRS

Considering the WRF-Chem setup reported in Table 3, it is important to remark that among the large number of chemistry packages actually available in WRF-Chem

distribution, calculation of aerosol optical properties is possible with `chem_opt = 300` (GOCART_SIMPLE configuration). This was very useful, as it allowed us to determine which of the S1 and S2 grain distributions is more appropriate for this particular case study (Table 2). This can be done by comparing the Aerosol Optical Depth (AOD) from the model output with the AERDB/AOD retrievals [55] described in Section 2.3. The GOCART aerosol model activates the WRF-Chem optical modules, which allows for calculation of plume optical properties such as the extinction coefficients at 0.55 µm (`extcof55`), from which the AOD_{055} can be calculated offline as follows:

$$AOD_{055}(x,y) = \sum_{i=z1}^{ztop} extcof55_i(x,y,z) * dz. \quad (2)$$

Here, the integration is performed from the bottom vertical level (z_1) up to the upper top level (z_{top}), with Δz as the depth of the layer between levels i and $i-1$. Our analysis starts by comparing the daily averaged AERDB [55] (Figure 6) products for the AOD_{055} at 0.55 µm with the corresponding simulated quantity calculated with Equation (1). In Figure 8, we report the numerical AOD obtained for GCTS2 (left column) and GCTS1 (right column) configurations (see Table 3). The first row (panels a,b) is calculated for 19:00 UTC on 23 April, the second row (panels c,d) for 19:00 UTC on 24 April, and the third row (panels e,f) for 19:00 UTC on 25 April. It is immediately evident that (i) GCTS2 simulation overestimates the AOD, and (ii) the GCTS1 simulation provides a good reproduction of the peak values and spatial pattern of the AERDB/AOD data. This is evident when comparing Figure 8b with Figure 6a for 23 April and Figure 8d with Figure 6b for 24 April. These results indicate that the S2 total grain distribution produces a considerable overestimation of the quantity of ash in the numerical domain, while the GCTS1 setup and associated S1 grain distribution, though still producing an overestimate, appears to be more appropriate for this situation. To analyze each day separately, we complement Figure 8 with Figures A1–A5 reported in Appendix A. This helps in the analysis of different vertical layers; specifically, it can help to explain the role of synoptic systems in the propagation of ash clouds. Figure 8b depicts the model AOD_{055} on 23 April at 19:00 UTC for the GCTS1 run. A very good reproduction of the experimental AERDB/AOD [55] is evident in Figure 6a in terms of both the spatial pattern and intensity. Figures A1 and A2 suggest that most of the p10 ash content is in the upper levels (17–20 km) due to the effect of plume lifting induced by the volcanic eruption. At lower levels, the ash plume spreads toward the Pacific Ocean due to the high pressure along the continental coast, which favors southwest transport and allows the plume to cross the Andes. By the end of 23 April, the average southwesterly winds between 500 hPa and 200 hPa (middle and upper levels) have advected the volcanic ash plume across the Andes towards Argentina. Figure 8d depicts the GCTS1 model prediction for 24 April. It can be noticed that the plume has now traveled for more than 2000 km in the northeast direction, reaching Uruguay and the city of Buenos Aires. This is also reported by AERDB/AOD ([55]; Figure 6b) and BTD (Figure 7b). The propagation of the plume at high levels of the atmosphere is coherent with the 200 hPa upper level flow, as seen in Figure 2d. The highest concentration is observed at high levels due to the eruption activity and the plume advection on 23 April, which intensely transports these particulates to higher levels. Meanwhile, in the Pacific region, the stability generated by stable anticyclonic atmospheric flow maintains the same AOD_{055} transport pattern as observed on 23 April. The maps for 25 April are reported in Figures 8f and A3. It is noteworthy to highlight the further displacement of the volcanic plume in the northeast direction towards the Atlantic coasts of Argentina, Uruguay, and southern Brazil. This is caused by displacement of the trough in the upper troposphere (Figure 3d) effectively transporting these particulates. The simulations indicate that the plume reaches densely populated regions of Brazil such as São Paulo and Rio de Janeiro.

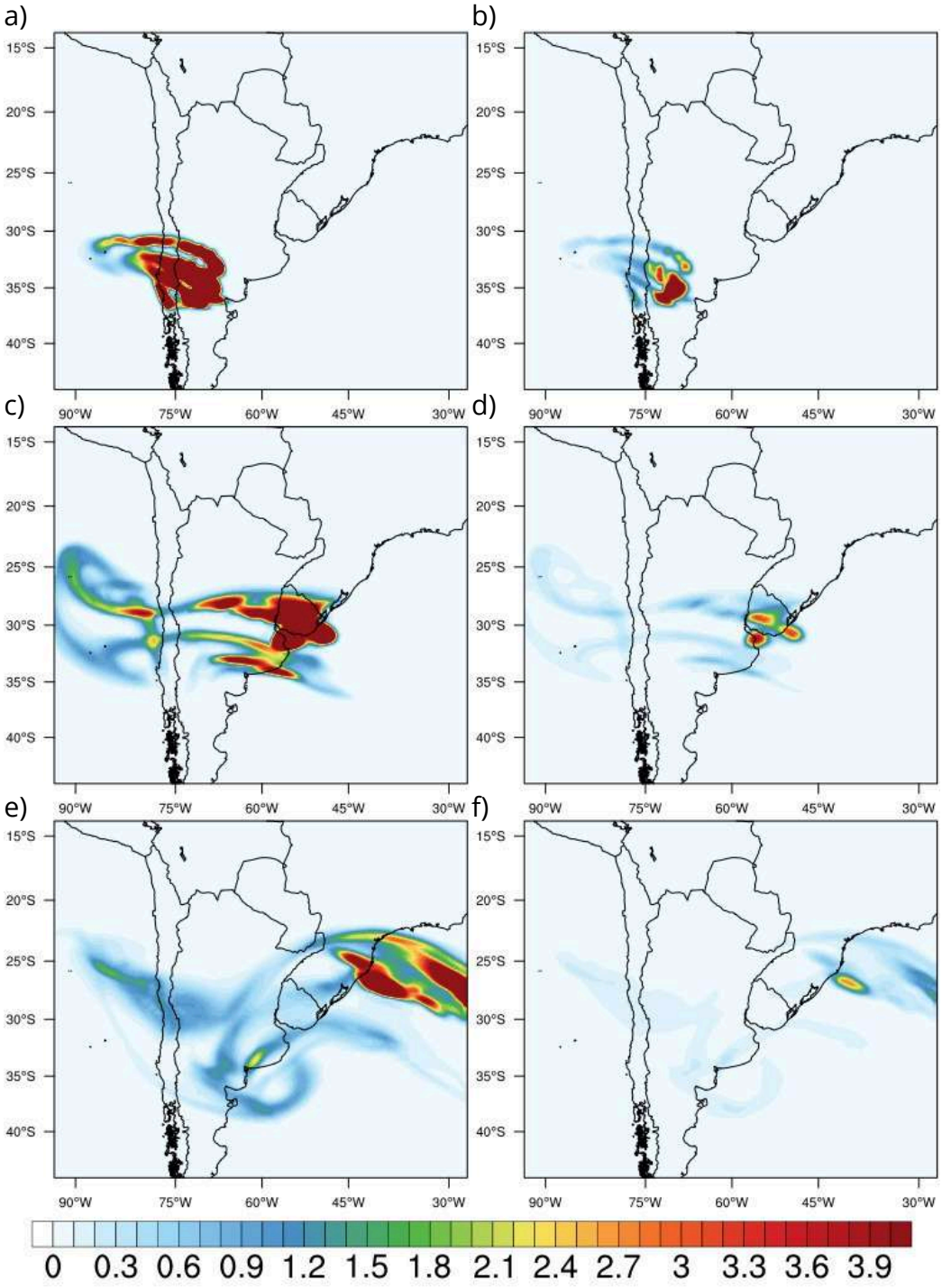

Figure 8. Model maps of AOD at 0.55 µm on 23 April for (**a**) AOD-GCTS2 and (**b**) AOD-GCTS1; on 24 April for (**c**) AOD-GCTS2 and (**d**) AOD-GCTS1; and on 25 April for (**e**) AOD-GCTS2 and (**f**) AOD-GCTS1.

In the following days, the volcanic plume moved in the direction of the African continentwhich was reached at the end of April 2015 [14]. The data presented from the average AOD representation in the GCTS1 setup corroborate with observations from both the BTD (Section 2.4) and AOD values from VIIRS (Section 2.3), where the first day of the event shows a higher concentration of particulates in the region near the volcano along with effective transport to higher levels of the atmosphere. On the second day post-eruption, meteorological events in both the upper and lower levels directly impacted the transport

and concentration of the particulates, indicating displacement in higher concentrations to the regions over Argentina and Uruguay. During the day of 25 April, the influence of a trough transported these particulates over the southeastern region of Brazil at high levels, while the high pressure at lower levels favored the maintenance of these particulates in lower concentrations over central Argentina. The GCTS2 simulation manages to represent the transport of these particulates even at reasonably high concentrations, indicating that the model is able to successfully represent the meteorological systems acting over the region during the event. The conclusion that may be drawn from these results is that the optical properties are better reproduced by the GCTS1 setup; this means that in terms of the S-type granule range, the S1 distribution with a lower mass of fine-size particles is better suited for simulating the transport of the Calbuco volcanic plume.

3.1.2. OMI/OMPS

The Ozone Mapper and Profiler Suite (OMPS) Limb Profiler (LP) onboard the Suomi National Polar Partnership (NPP) spacecraft provided the best plume coverage for the Calbuco eruption in April 2015. The estimated SO_2 emission from the first overpasses following the eruption is 0.2 Tg. On the web page of the Atmospheric Chemistry and Dynamics Laboratory of the Goddard Space Flight Center (NASA), it is possible to download Sulfur Dioxide Image Galleries for a large set of world volcanoes for the time period from 2011 to the present. In particular, concerning the Calbuco April 2015 eruption, there are reported high-resolution composites of the Ozone Monitoring Instrument (OMI) onboard the Aura spacecraft and OMPS images. The SO_2 emissions were estimated by the SERNAGEOMIN (Chilean Geology Service) to be 0.133×10^9 kg h^{-1} for the first eruption and 0.4×10^9 kg h^{-1} for the second (Table 1). This may be a critical point, as these estimations should be replaced by direct measurements obtained via remote sensing techniques to provide a realistic time-varying emission rate of SO_2 [21]. To check the quality of our WRF-Chem simulation of the transport of SO_2 in South America, we compared model outputs with satellite retrievals. The composite OMI+OMPS SO_2 retrievals for 23 April are depicted in Figure 9; it can be seen that the columnar SO_2 distribution after the two main eruptions is dislocated from the Pacific Ocean (5 DU) to internal Argentina with a concentration on the order of 20 DU and peak value of 47.35 DU at longitude 71.38°W and latitude 36.55°S. The WRF-Chem model output reported in Figure 9b reproduces both the spatial pattern (with a slight overestimation) and the position and intensity of the peak value.

As discussed in previous sections, on 24 April the SO_2 volcanic plume was transported towards Uruguay and the city of Buenos Aires, with maximum values around 40 DU. A long tail reached the Pacific Ocean with a concentration on the order of 10 DU. Comparison between the model (Figure 10b) and satellite retrieval (Figure 10a) data reveals an optimal comparison for the spatial pattern and concentration of columnar SO_2.

Two days after the first eruption, on 25 April, the SO_2 plume moved further in the northeast direction, with the largest part along the offshore coast of southern Brazil (Figure 11a) with more than 15 DU. Again, the WRF-Chem predictions are in good agreement with experimental data (Figure 11b) considering the spatial distribution and the columnar concentration with a maximum in the range of 15–20 DU.

Finally, on 26 April the SO_2 plume moved offshore in the direction of the African continent (Figure 12a), and reached the Indian Ocean one week after the first eruption [14]. The comparison between the SO_2 dispersion maps simulated by the model and the data observed by OMI-OMPS show fair agreement, but with a slight overestimation of the simulated concentration of SO_2 (Figure 12b). This may be caused by an overestimation of the SO_2 experimental emission rate.

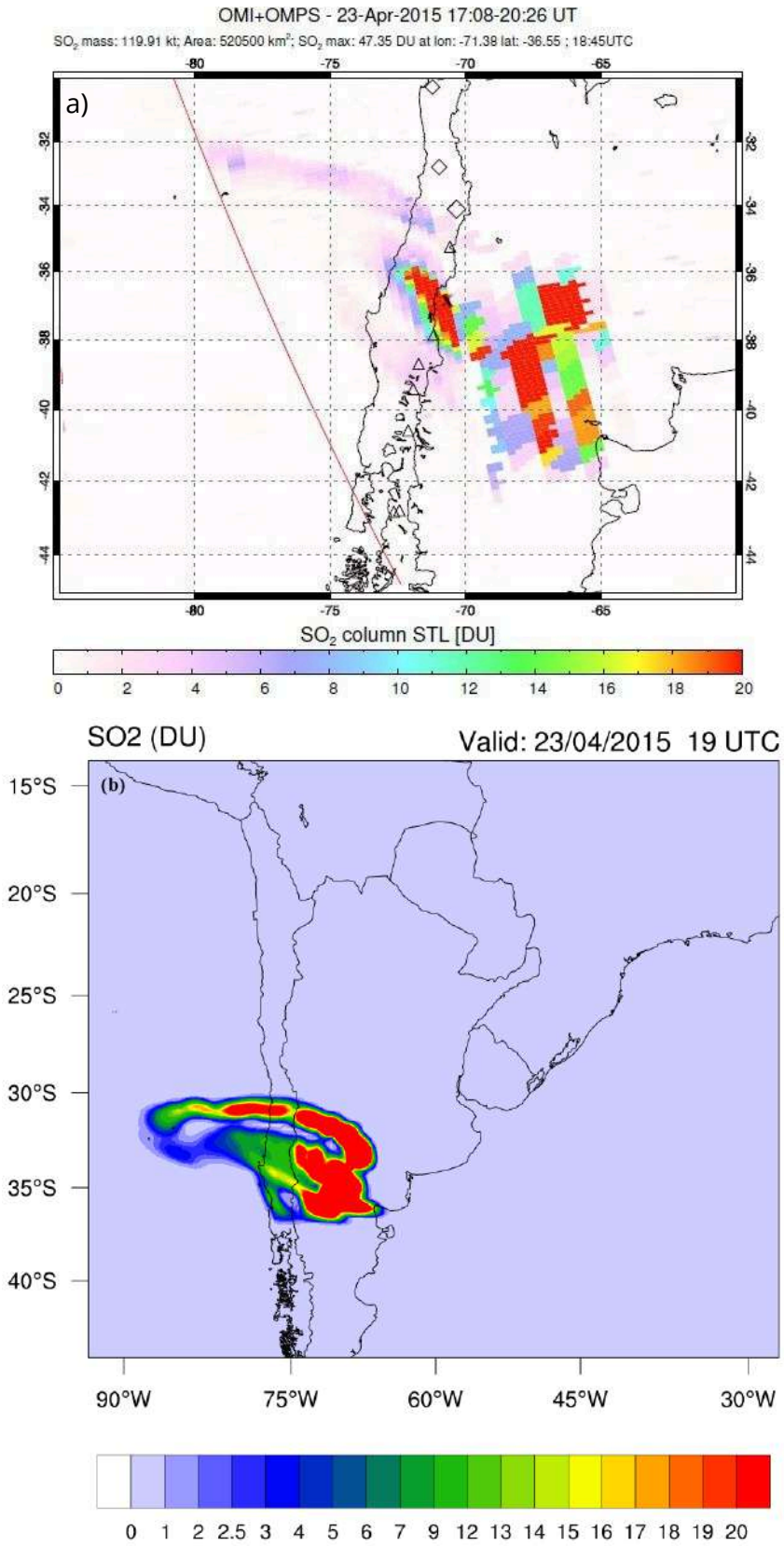

Figure 9. (**a**) OMI+OMPS SO_2 retrievals in Dobson Units for 23 April 2015 between 17:08 and 20:26 UTC (source: https://so2.gsfc.nasa.gov/ (accessed on 1 October 2024)) and (**b**) WRF-Chem SO_2 prediction for 23 April at 19 UTC.

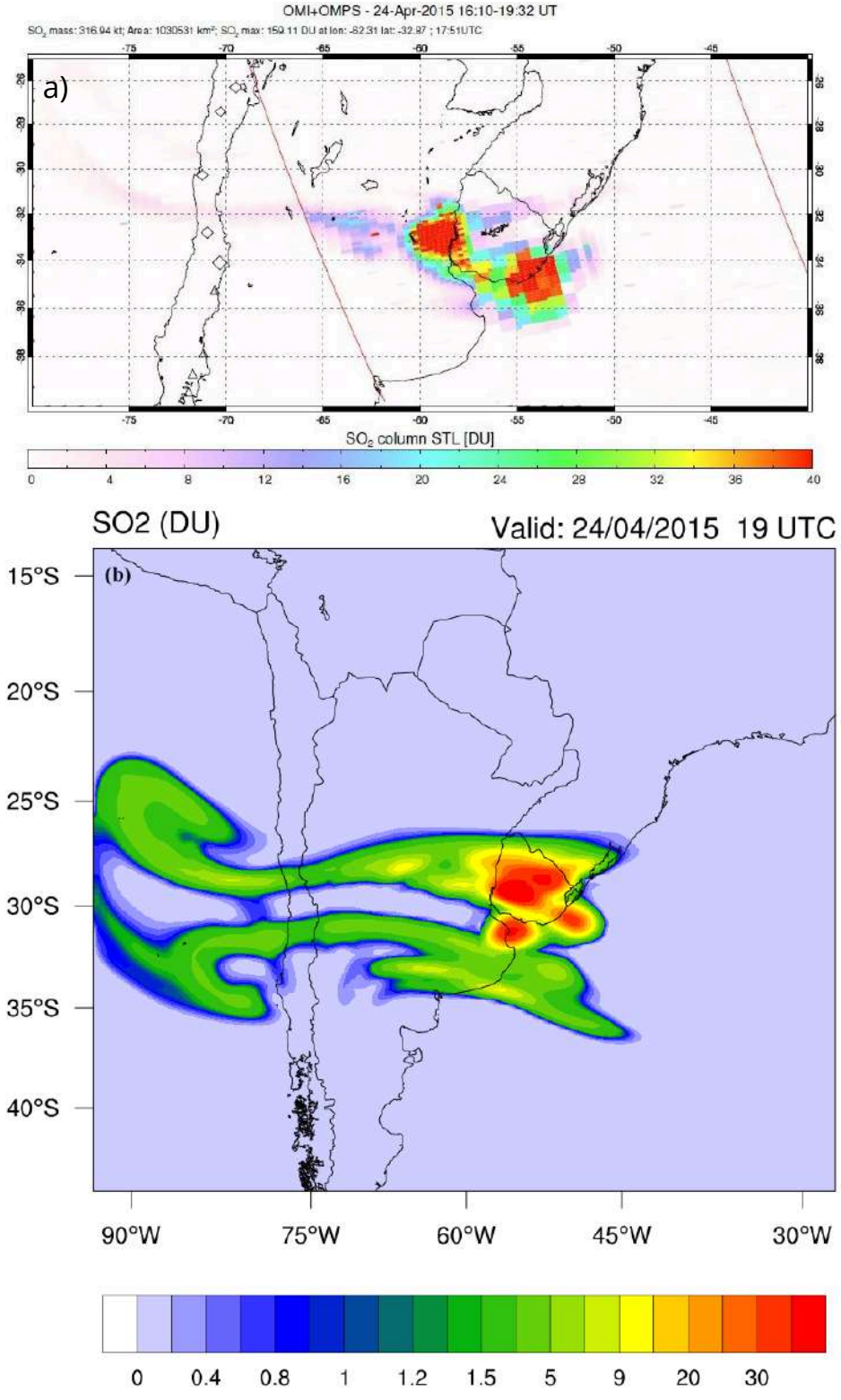

Figure 10. (**a**) OMI+OMPS SO_2 retrievals in Dobson Units for 24 April 2015 between 16:10 and 19:32 UTC (source: https://so2.gsfc.nasa.gov/ (accessed on 1 October 2024)) and (**b**) WRF-Chem SO_2 prediction for 24 April at 19 UTC.

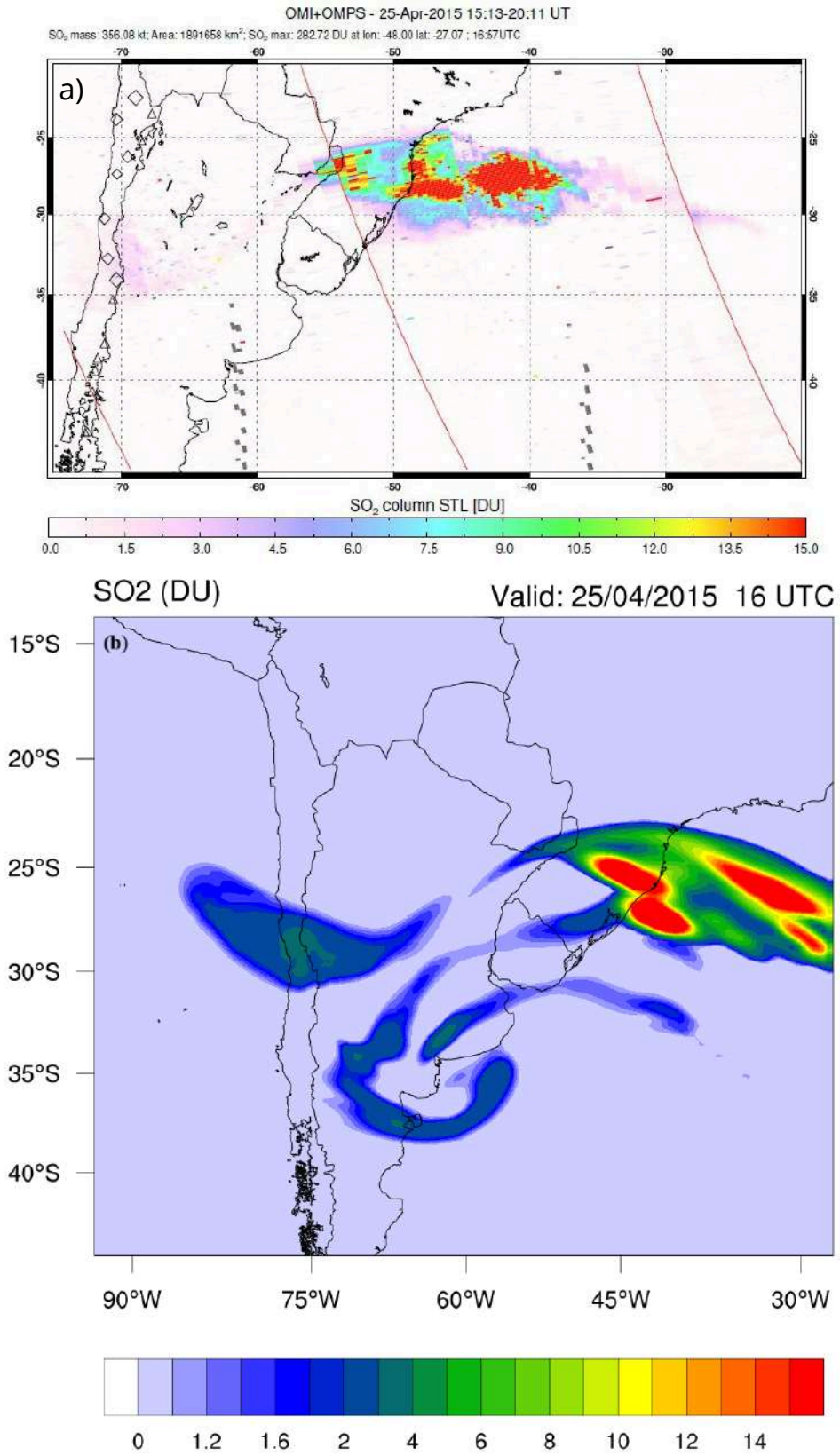

Figure 11. (**a**)OMI+OMPS SO_2 retrievals in Dobson Units for 25 April 2015 between 15:13 and 20:11 UTC (source: https://so2.gsfc.nasa.gov/ (accessed on 1 October 2024)) and (**b**) WRF-Chem SO_2 prediction for 25 April at 16 UTC.

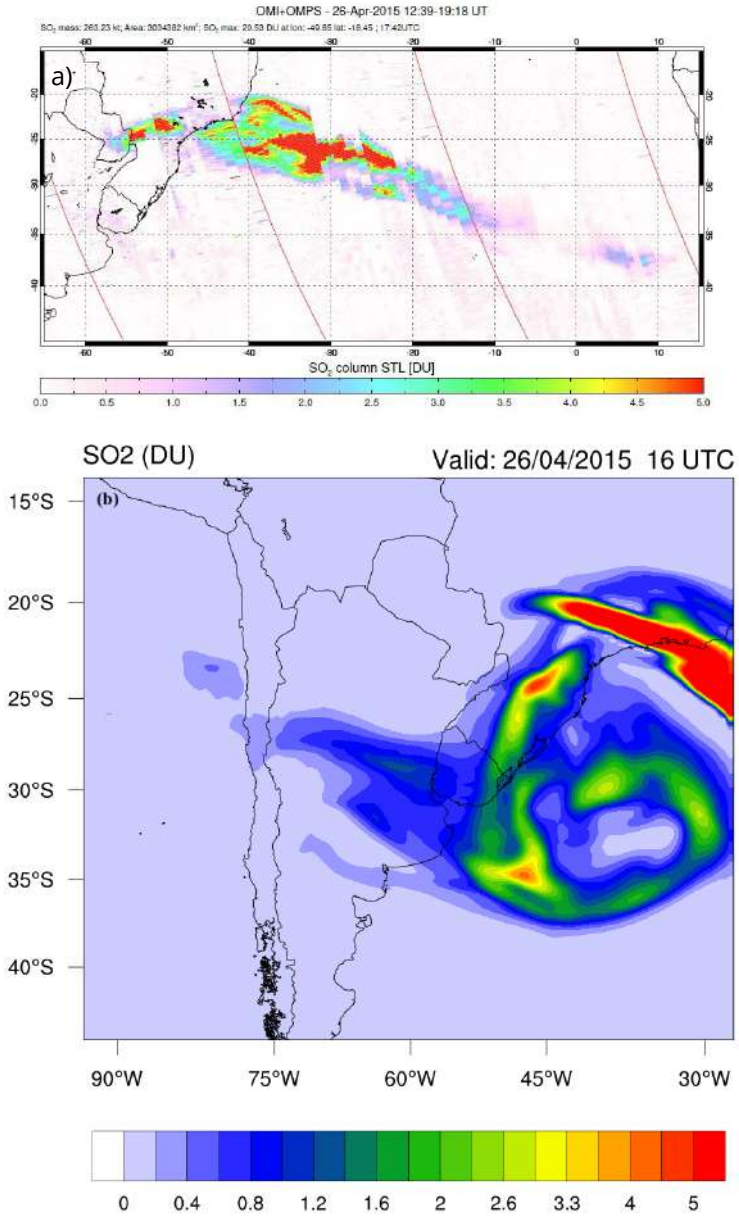

Figure 12. (**a**) OMI+OMPS SO_2 retrievals in Dobson Units for 26 April 2015 between 12:39 and 19:18 UTC (source: https://so2.gsfc.nasa.gov/ (accessed on 1 October 2024)) and (**b**) WRF-Chem SO_2 prediction for 26 April at 16 UTC.

4. Conclusions

In this study, we used the WRF-Chem model [38] to describe two eruptions of the Calbuco volcano that occurred on 22–23 April 2015. Using the model configuration under the GOCART speciation for aerosol [39] allowed us to activate the optical modules, from which it is possible to calculate (offline) the model AOD, which can then be compared with satellite retrievals, in this case AERDB_D3_VIIRS_SNPP. Two different distributions of the ash granulometry from the WRF-Chem database [22] were tested against experimental satellite data to find the best option for Calbuco. To the best of our knowledge, this study represents the first application of the WRF-Chem package to model eruptions from Calbuco. We have analyzed the transport of ash in the numerical domain in terms of synoptic meteorological conditions that are peculiar to the South American continent, and have evidenced the role of the Andes Mountain range in lifting the ash plume into the high troposphere and blocking the zonal winds [27,37]. In this context, the synoptic characterization during the simulated period from 22–26 April can be divided into lower and upper levels. We

have verified that the plume managed to reach higher levels of the atmosphere during the more intense ejection of the second eruption [17]. In addition, the southwestward wind at high levels favored intensification of vertical movement, helping the plume to reach the upper troposphere. In the following days, the displacement of a trough over the regions of Argentina, Uruguay, and Brazil assisted in the propagation of this plume [29]. When observing the lower portion of the atmosphere, the presence of a high-pressure system offshore of the Chilean coast caused the transport of ash toward the Pacific Ocean during the first day. In the following days, the influence of a high-pressure system forming over the northern region of Argentina favored propagation of the plume over the central region, reaching the cities of Buenos Aires and Montevideo. On 25 April, the confluence of eastward winds due to the emergence of a low-pressure system to the south of the continent intensified transport over the northern regions of Uruguay and southern Brazil. Based on our analysis, the WRF-Chem model can successfully represent these synoptic systems, which were of paramount importance during the event. The transport of the ash plume was analyzed by combining information from our synoptic analysis and experimental data from the VIIRS sensor onboard the SUOMI spacecraft using L2 products at both visible (AOD) [59] and IR (BTD) [58] wavelengths. The principal results of this study may be summarized as follows:

- From a meteorology perspective, the WRF-ARW core of the WRF-Chem model successfully reproduced the synoptic patterns responsible for ash transport. The fine ash from the two massive eruptions of Mount Calbuco contaminated the airspace around the volcano within a radius of about 4000 km in a few days. This is a very important aspect that needs to be considered; in fact, the complexity of the problem requires an integrated approach consisting of an online coupling between meteorology and aerosols.
- The comparison between model and AOD utilizing the experimental data allowed us to select the optimal granulometry distribution (S1), which may be important in subsequent studies.
- Our comparison between the SO_2 dispersion maps simulated by the model and the OMI-OMPS retrievals report good agreement, likely with a slight overestimation of the simulated concentration of SO_2. This discrepancy is likely caused by an overestimation of the SO_2 emission rate.

This study demonstrates the feasibility of using the WRF-Chem model under volcanic configuration to reproduce the spatial patterns of ash and SO_2. In this particular complex test case, we have demonstrated the good performance of this model in reproducing the synoptic patterns and consequent transport of volcanic ashes and SO_2, highlighting the need for this kind of coupled modeling between meteorology and aerosols. This successful modeling further allows for the activation of feedback between aerosols and both radiation (direct effect) and cloud microphysics (indirect effect), which will be the object of our subsequent studies.

Author Contributions: Conceptualization, D.L.d.B., U.R. and V.A.; investigation, U.R., D.L.d.B. and V.A.; methodology, D.L.d.B., U.R., V.A. and F.S.P.; software, U.R.; validation, D.L.d.B., U.R. and V.A.; formal analysis, D.L.d.B., U.R., V.A., F.S.P., D.K.P., L.A.S. and L.B.; visualization D.L.d.B., U.R. and F.G.; writing—original draft, D.L.d.B., U.R. and V.A.; writing—review and editing, L.A.S. and L.B. All authors have read and agreed to the published version of the manuscript.

Funding: This study is supported by CAPES (Coordination of Improvement of Higher Education Personnel) of the research activity (B2IST "Biomass Burning and Impacts in the Southern Tropics", registered under no. 88881.694487/2022-01, and AEROBI "AERosol Observations over Brazil and Impacts", registered under no. 88881.711960/2022-01).

Data Availability Statement: All codes in this study used to initiate and run the model are publicly accessible on GitHub (WRF: https://github.com/douglima8/WRF_ASH), accessed on 26 November 2024.

Acknowledgments: We thank the National Research Council−Institute of Atmospheric Sciences and Climate of Italy for her generous help with the setup of model.

Conflicts of Interest: The authors declare that they have no known competing financial interests or personal relationships that could have influenced or appeared to influence the work reported in this paper.

Appendix A

The following Figures A1−A5 report the vertical integration of the p10 variable (from GCTS1 simulation), which is provided in units of µg m^{-2} when scaled with the air density. It is calculated as the sum of finest ash bins in the following way:

$$p10 = 0.5 * vash_8 + vash_9 + 0.5 * vash_{10}. \quad \text{(A1)}$$

In each figure, panel a refers to the integration between 0−17 km and panel b to the integration between 17−20 km.

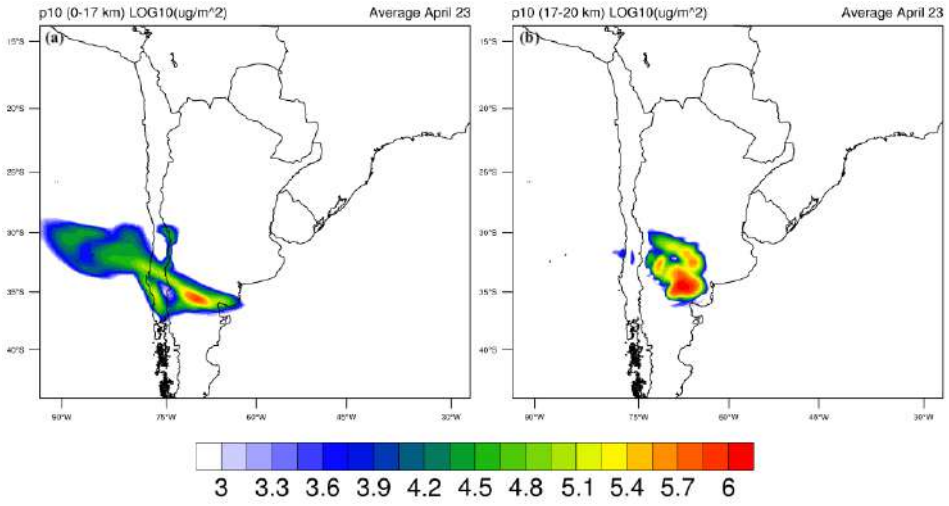

Figure A1. Daily averaged vertical integrated concentration (p10) between (**a**) 0−17 km and (**b**) 17−20 km for23 April; units are µg m^{-2}.

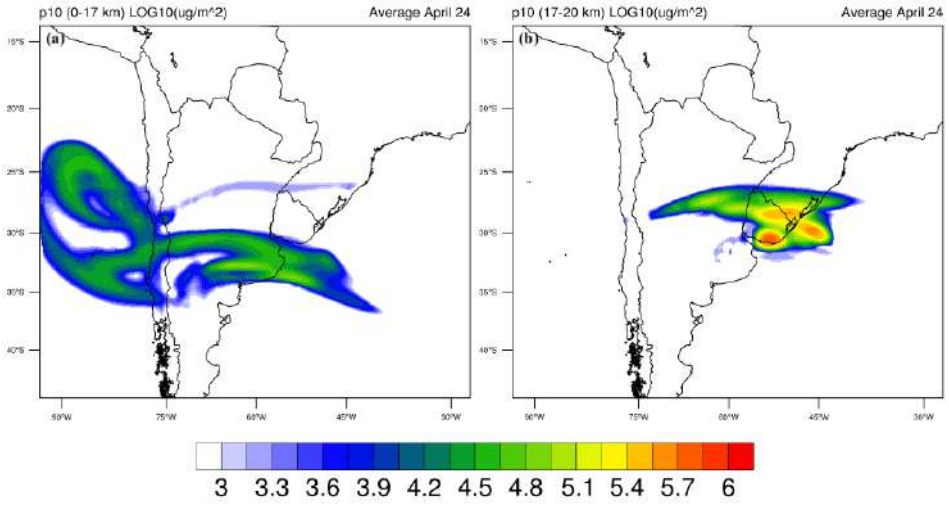

Figure A2. Daily averaged vertical integrated concentration (p10) between (**a**) 0−17 km and (**b**) 17−20 km for 24 April; units are µg m^{-2}.

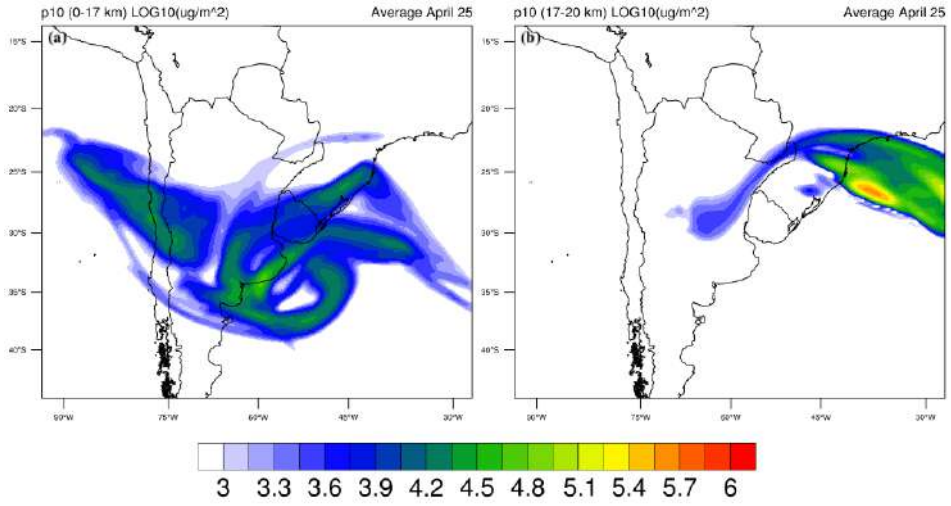

Figure A3. Daily averaged vertical integrated concentration (p10) between (**a**) 0−17 km and (**b**) 17−20 km for 25 April; units are μg m^{-2}.

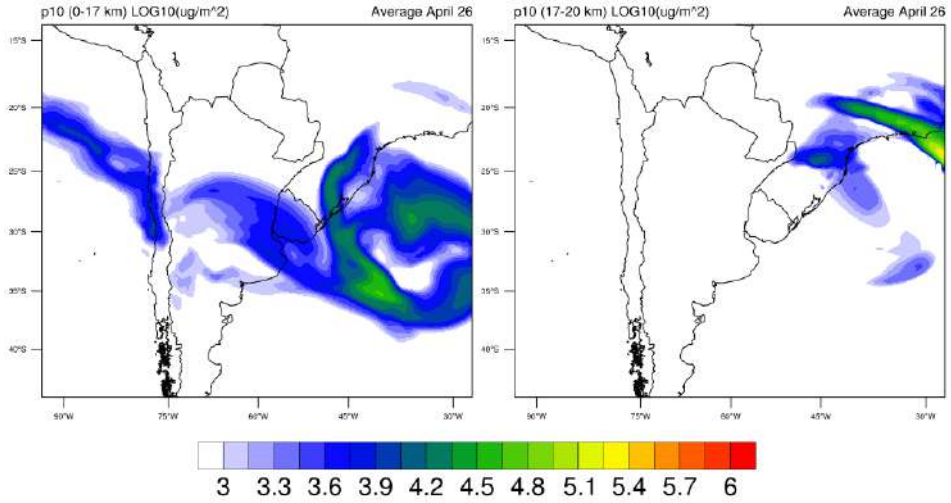

Figure A4. Daily averaged vertical integrated concentration (p10) between (**a**) 0–17 km and (**b**) 17–20 km for 26 April; units are μg m^{-2}.

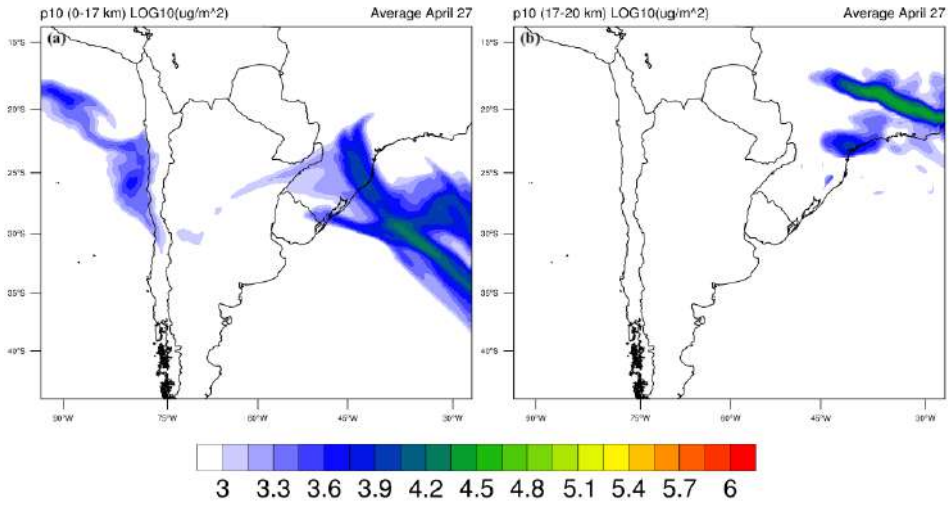

Figure A5. Daily averaged vertical integrated concentration (p10) between (**a**) 0–17 km and (**b**) 17–20 km for April 27; units are μg m^{-2}.

Appendix B

To better understand the moments leading up to the eruption, our analysis used modeled data for temperature and dew point temperature profiles to assess the stability of the atmospheric layers. For this purpose, skew-T diagrams are presented for every 3 h, starting at 00:00 UTC on the 22 April and continuing until 21:00 UTC on the same day (the time of the first recorded eruption). There are two basic lines plotted on a Skew-T, from which we can derive much information. These represent the dew point, which is calculated from the relative humidity (green, left line) and air temperature (red, right line). While air temperature generally decreases with height, this decrease is neither uniform nor consistent, as the air temperature sometimes remains the same or increases with height. When the normal temperature decrease is "inverted" and the temperature increases with height, this is called a temperature inversion. This skew-T is set for the volcano's coordinates.

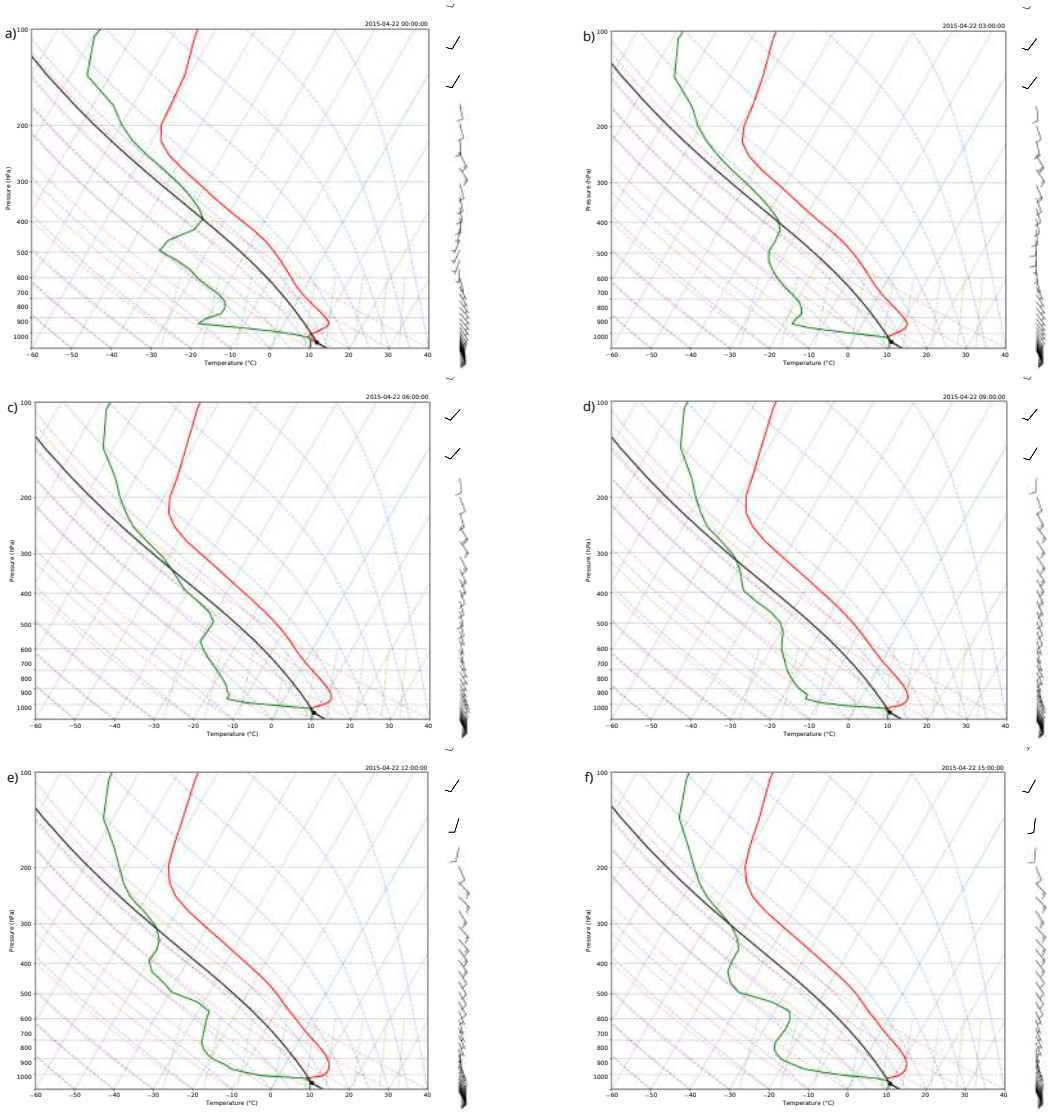

Figure A6. *Cont*.

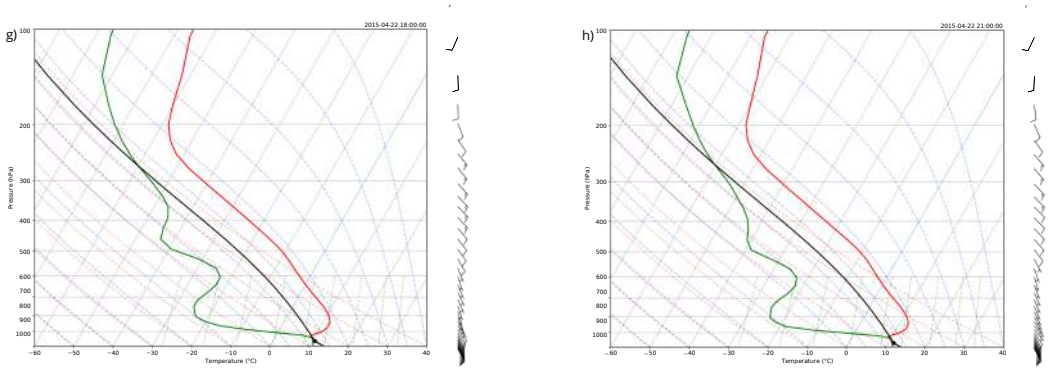

Figure A6. Skew-T for the Calbuco volcano region prior to the first eruption; the red line indicates the temperature, the green line the dew point temperature, and the black line the Lifted Condensation Level (LCL). The barbs on the right side indicate the direction and speed of the wind. (**a**) 00:00 ; (**b**) 03:00; (**c**) 06:00; (**d**) 09:00; (**e**) 12:00; (**f**) 15:00; (**g**) 18:00; (**h**) 21:00.

References

1. Ramaswamy, V.; Collins, W.; Haywood, J.; Lean, J.; Mahowald, N.; Myhre, G.; Naik, V.; Shine, K.P.; Soden, B.; Stenchikov, G.; et al. Radiative forcing of climate: The historical evolution of the radiative forcing concept, the forcing agents and their quantification, and applications. *Meteorol. Monogr.* **2019**, *59*, 14.1–14.101. [CrossRef]
2. Charlson, R.J.; Schwartz, S.; Hales, J.; Cess, R.D.; Coakley, J., Jr.; Hansen, J.; Hofmann, D. Climate forcing by anthropogenic aerosols. *Science* **1992**, *255*, 423–430. [CrossRef] [PubMed]
3. Twomey, S. The influence of pollution on the shortwave albedo of clouds. *J. Atmos. Sci.* **1977**, *34*, 1149–1152. [CrossRef]
4. Textor, C.; Graf, H.F.; Timmreck, C.; Robock, A. Emissions from volcanoes. In *Emissions of Atmospheric Trace Compounds*; Springer: Berlin/Heidelberg, Germany, 2004; pp. 269–303. [CrossRef]
5. Arghavani, S.; Rose, C.; Banson, S.; Lupascu, A.; Gouhier, M.; Sellegri, K.; Planche, C. The effect of using a new parameterization of nucleation in the WRF-Chem model on new particle formation in a passive volcanic plume. *Atmosphere* **2021**, *13*, 15. [CrossRef]
6. Tsigaridis, K.; Krol, M.; Dentener, F.; Balkanski, Y.; Lathiere, J.; Metzger, S.; Hauglustaine, D.; Kanakidou, M. Change in global aerosol composition since preindustrial times. *Atmos. Chem. Phys.* **2006**, *6*, 5143–5162. [CrossRef]
7. McCormick, M.P.; Thomason, L.W.; Trepte, C.R. Atmospheric effects of the Mt Pinatubo eruption. *Nature* **1995**, *373*, 399–404. [CrossRef]
8. Sellitto, P.; Podglajen, A.; Belhadji, R.; Boichu, M.; Carboni, E.; Cuesta, J.; Duchamp, C.; Kloss, C.; Siddans, R.; Bègue, N.; et al. The unexpected radiative impact of the Hunga Tonga eruption of 15 January 2022. *Commun. Earth Environ.* **2022**, *3*, 288. [CrossRef]
9. Stern, C.R.; Moreno, H.; López-Escobar, L.; Clavero, J.E.; Lara, L.E.; Naranjo, J.A.; Parada, M.A.; Skewes, M.A. Chilean volcanoes. *Geol. Soc. Lond.* **2007**. [CrossRef]
10. Newhall, C.G.; Self, S. The volcanic explosivity index (VEI) an estimate of explosive magnitude for historical volcanism. *J. Geophys. Res. Ocean.* **1982**, *87*, 1231–1238. [CrossRef]
11. González-Ferrán, O. Volcanes de Chile. Instituto Geográfico Militar. *Santiago* **1995**, *635*. Available online: https://books.google.fr/books?id=m2hdAAAAMAAJ (accessed on 1 October 2024)
12. Petit-Breuilh, M. *Cronologia Eruptiva Historica de los Volcanes Osorno y Calbuco, Andes del Sur (41°–41°30's)*; Servicio Nacional de Geología y Minería: Santiago, Chile, 1999.
13. Daga, R.; Guevara, S.R.; Poire, D.G.; Arribére, M. Characterization of tephras dispersed by the recent eruptions of volcanoes Calbuco (1961), Chaitén (2008) and Cordón Caulle Complex (1960 and 2011), in Northern Patagonia. *J. S. Am. Earth Sci.* **2014**, *49*, 1–14. [CrossRef]
14. Bègue, N.; Vignelles, D.; Berthet, G.; Portafaix, T.; Payen, G.; Jégou, F.; Bencherif, H.; Jumelet, J.; Vernier, J.P.; Lurton, T.; et al. Long-range transport of stratospheric aerosols in the Southern Hemisphere following the 2015 Calbuco eruption. *Atmos. Chem. Phys.* **2017**, *17*, 15019–15036. [CrossRef]
15. JS Lopes, F.; Silva, J.J.; Antuna Marrero, J.C.; Taha, G.; Landulfo, E. Synergetic aerosol layer observation after the 2015 calbuco volcanic eruption event. *Remote Sens.* **2019**, *11*, 195. [CrossRef]
16. Van Eaton, A.R.; Amigo, Á.; Bertin, D.; Mastin, L.G.; Giacosa, R.E.; González, J.; Valderrama, O.; Fontijn, K.; Behnke, S.A. Volcanic lightning and plume behavior reveal evolving hazards during the April 2015 eruption of Calbuco volcano, Chile. *Geophys. Res. Lett.* **2016**, *43*, 3563–3571. [CrossRef]
17. Romero, J.; Morgavi, D.; Arzilli, F.; Daga, R.; Caselli, A.; Reckziegel, F.; Viramonte, J.; Díaz-Alvarado, J.; Polacci, M.; Burton, M.; et al. Eruption dynamics of the 22–23 April 2015 Calbuco Volcano (Southern Chile): Analyses of tephra fall deposits. *J. Volcanol. Geotherm. Res.* **2016**, *317*, 15–29. [CrossRef]
18. Marzano, F.S.; Corradini, S.; Mereu, L.; Kylling, A.; Montopoli, M.; Cimini, D.; Merucci, L.; Stelitano, D. Multisatellite multisensor observations of a Sub-Plinian volcanic eruption: The 2015 Calbuco explosive event in Chile. *IEEE Trans. Geosci. Remote Sens.* **2018**, *56*, 2597–2612. [CrossRef]

19. Mastin, L.G.; Van Eaton, A.R. Comparing simulations of umbrella-cloud growth and ash transport with observations from Pinatubo, Kelud, and Calbuco volcanoes. *Atmosphere* **2020**, *11*, 1038. [CrossRef]
20. Schwaiger, H.F.; Denlinger, R.P.; Mastin, L.G. Ash3d: A finite-volume, conservative numerical model for ash transport and tephra deposition. *J. Geophys. Res. Solid Earth* **2012**, *117*. [CrossRef]
21. Castorina, G.; Semprebello, A.; Gattuso, A.; Salerno, G.; Sellitto, P.; Italiano, F.; Rizza, U. Modelling Paroxysmal and Mild-Strombolian Eruptive Plumes at Stromboli and Mt. Etna on 28 August 2019. *Remote Sens.* **2023**, *15*, 5727. [CrossRef]
22. Stuefer, M.; Freitas, S.; Grell, G.; Webley, P.; Peckham, S.; McKeen, S.; Egan, S. Inclusion of ash and SO_2 emissions from volcanic eruptions in WRF-Chem: Development and some applications. *Geosci. Model Dev.* **2013**, *6*, 457–468. [CrossRef]
23. Stenchikov, G.; Ukhov, A.; Osipov, S. Modeling of Instantaneous and Adjusted Radiative Forcing of the 2022 Hunga Volcano Explosion. In Proceedings of the EGU General Assembly 2024, Vienna, Austria, 14–19 April 2024. [CrossRef]
24. Fast, J.D.; Gustafson, W.I., Jr.; Easter, R.C.; Zaveri, R.A.; Barnard, J.C.; Chapman, E.G.; Grell, G.A.; Peckham, S.E. Evolution of ozone, particulates, and aerosol direct radiative forcing in the vicinity of Houston using a fully coupled meteorology-chemistry-aerosol model. *J. Geophys. Res. Atmos.* **2006**, *111*. [CrossRef]
25. Stenchikov, G.; Lahoti, N.; Diner, D.J.; Kahn, R.; Lioy, P.J.; Georgopoulos, P.G. Multiscale plume transport from the collapse of the World Trade Center on September 11, 2001. *Environ. Fluid Mech.* **2006**, *6*, 425–450. . [CrossRef]
26. Seluchi, M.E.; Marengo, J.A. Tropical–midlatitude exchange of air masses during summer and winter in South America: Climatic aspects and examples of intense events. *Int. J. Climatol. A J. R. Meteorol. Soc.* **2000**, *20*, 1167–1190. [CrossRef]
27. Marengo, J.A.; Seluchi, M.E. Tropical mid-latitude exchange of air masses in South America. Part I: Some climatic aspects. In Proceedings of the Trabajo presentado en el VIII Congreso Latinoamericano e Ibérico de Meteorología y X Congresso Brasileiro de Meteorologia, Brasilia, Brasil, 20 January, 1998.
28. Gan, M.A.; Rao, V.B. The influence of the Andes Cordillera on transient disturbances. *Mon. Weather Rev.* **1994**, *122*, 1141–1157. [CrossRef]
29. Seluchi, M.E.; Garreaud, R.; Norte, F.A.; Saulo, A.C. Influence of the subtropical Andes on baroclinic disturbances: A cold front case study. *Mon. Weather Rev.* **2006**, *134*, 3317–3335. [CrossRef]
30. Satyamurty, P.; Dos Santos, R.P.; Lems, M.A.M. On the stationary trough generated by the Andes. *Mon. Weather Rev.* **1980**, *108*, 510–520. [CrossRef]
31. Ivy, D.J.; Solomon, S.; Kinnison, D.; Mills, M.J.; Schmidt, A.; Neely III, R.R. The influence of the Calbuco eruption on the 2015 Antarctic ozone hole in a fully coupled chemistry-climate model. *Geophys. Res. Lett.* **2017**, *44*, 2556–2561. [CrossRef]
32. Phillips, N.A. The general circulation of the atmosphere: A numerical experiment. *Q. J. R. Meteorol. Soc.* **1956**, *82*, 123–164. [CrossRef]
33. Pinheiro, H.R.; Hodges, K.I.; Gan, M.A.; Ferreira, N.J. A new perspective of the climatological features of upper-level cut-off lows in the Southern Hemisphere. *Clim. Dyn.* **2017**, *48*, 541–559. [CrossRef]
34. Hakim, G.J.; Uccellini, L.W. Diagnosing coupled jet-streak circulations for a northern plains snow band from the operational nested-grid model. *Weather Forecast.* **1992**, *7*, 26–48. [CrossRef]
35. Uccellini, L.W.; Kocin, P.J. The interaction of jet streak circulations during heavy snow events along the east coast of the United States. *Weather Forecast.* **1987**, *2*, 289–308. [CrossRef]
36. Arzilli, F.; Morgavi, D.; Petrelli, M.; Polacci, M.; Burton, M.; Di Genova, D.; Spina, L.; La Spina, G.; Hartley, M.E.; Romero, J.E.; et al. The unexpected explosive sub-Plinian eruption of Calbuco volcano (22–23 April 2015; southern Chile): Triggering mechanism implications. *J. Volcanol. Geotherm. Res.* **2019**, *378*, 35–50. [CrossRef]
37. Seluchi, M.E.; Norte, F.A.; Satyamurty, P.; Chou, S.C. Analysis of three situations of the foehn effect over the Andes (zonda wind) using the Eta–CPTEC regional model. *Weather Forecast.* **2003**, *18*, 481–501. [CrossRef]
38. Grell, G.A.; Peckham, S.E.; Schmitz, R.; McKeen, S.A.; Frost, G.; Skamarock, W.C.; Eder, B. Fully coupled "online" chemistry within the WRF model. *Atmos. Environ.* **2005**, *39*, 6957–6975. [CrossRef]
39. Chin, M.; Rood, R.B.; Lin, S.J.; Müller, J.F.; Thompson, A.M. Atmospheric sulfur cycle simulated in the global model GOCART: Model description and global properties. *J. Geophys. Res. Atmos.* **2000**, *105*, 24671–24687. [CrossRef]
40. Mastin, L.G.; Guffanti, M.; Servranckx, R.; Webley, P.; Barsotti, S.; Dean, K.; Durant, A.; Ewert, J.W.; Neri, A.; Rose, W.I.; et al. A multidisciplinary effort to assign realistic source parameters to models of volcanic ash-cloud transport and dispersion during eruptions. *J. Volcanol. Geotherm. Res.* **2009**, *186*, 10–21. [CrossRef]
41. Steensen, T.; Stuefer, M.; Webley, P.; Grell, G.; Freitas, S. Qualitative comparison of Mount Redoubt 2009 volcanic clouds using the PUFF and WRF-Chem dispersion models and satellite remote sensing data. *J. Volcanol. Geotherm. Res.* **2013**, *259*, 235–247. [CrossRef]
42. Scollo, S.; Del Carlo, P.; Coltelli, M. Tephra fallout of 2001 Etna flank eruption: Analysis of the deposit and plume dispersion. *J. Volcanol. Geotherm. Res.* **2007**, *160*, 147–164. [CrossRef]
43. Rose, W.I.; Durant, A.J. Fine ash content of explosive eruptions. *J. Volcanol. Geotherm. Res.* **2009**, *186*, 32–39. [CrossRef]
44. Freitas, S.R.; Longo, K.M.; Alonso, M.A.; Pirre, M.; Marécal, V.; Grell, G.; Stockler, R.; Mello, R.; Sánchez Gácita, M. PREP-CHEM-SRC–1.0: A preprocessor of trace gas and aerosol emission fields for regional and global atmospheric chemistry models. *Geosci. Model Dev.* **2011**, *4*, 419–433. [CrossRef]

45. Environmental Prediction/National Weather Service/NOAA/US Department of Commerce, N.C. NCEP GDAS/FNL 0.25 Degree Global Tropospheric Analyses and Forecast Grids, Research Data Archive at the National Center for Atmospheric Research, Computational and Information Systems Laboratory. National Centers for Environmental Prediction, National Weather Service, NOAA, U.S. Department of Commerce. 2015. Available online: https://rda.ucar.edu/datasets/d083003/ (accessed on 19 November 2024).
46. Sparks, R.S.J.; Bursik, M.; Carey, S.; Gilbert, J.; Glaze, L.; Sigurdsson, H.; Woods, A. *Volcanic Plumes*; John Wiley & Sons, Inc.: Hoboken, NJ, USA, 1997.
47. Vidal, L.; Nesbitt, S.W.; Salio, P.; Farias, C.; Nicora, M.G.; Osores, M.S.; Mereu, L.; Marzano, F.S. C-band dual-polarization radar observations of a massive volcanic eruption in South America. *IEEE J. Sel. Top. Appl. Earth Obs. Remote Sens.* **2017**, *10*, 960–974. [CrossRef]
48. Pardini, F.; Burton, M.; Arzilli, F.; La Spina, G.; Polacci, M. SO_2 emissions, plume heights and magmatic processes inferred from satellite data: The 2015 Calbuco eruptions. *J. Volcanol. Geotherm. Res.* **2018**, *361*, 12–24. [CrossRef]
49. Olson, J.B.; Kenyon, J.S.; Angevine, W.; Brown, J.M.; Pagowski, M.; Sušelj, K. *A Description of the MYNN-EDMF Scheme and the Coupling to Other Components in WRF–ARW*; Earth System Research Laboratory (U.S.) Global Systems Division: Boulder, CO, USA, 2019, Volume 61. [CrossRef]
50. Olson, J.B.; Smirnova, T.; Kenyon, J.S.; Turner, D.D.; Brown, J.M.; Zheng, W.; Green, B.W. *A Description of the MYNN Surface-Layer Scheme*; Earth System Research Laboratory (U.S.) Global Systems Division: Boulder, CO, USA, 2021, Volume 67. [CrossRef]
51. Smirnova, T.G.; Brown, J.M.; Benjamin, S.G.; Kenyon, J.S. Modifications to the rapid update cycle land surface model (RUC LSM) available in the weather research and forecasting (WRF) model. *Mon. Weather Rev.* **2016**, *144*, 1851–1865. [CrossRef]
52. Nakanishi, M.; Niino, H. An improved Mellor–Yamada level-3 model with condensation physics: Its design and verification. *Bound. Layer Meteorol.* **2004**, *112*, 1–31. [CrossRef]
53. Morrison, H.; Thompson, G.; Tatarskii, V. Impact of cloud microphysics on the development of trailing stratiform precipitation in a simulated squall line: Comparison of one-and two-moment schemes. *Mon. Weather Rev.* **2009**, *137*, 991–1007. [CrossRef]
54. Morrison, H.; Milbrandt, J.A.; Bryan, G.H.; Ikeda, K.; Tessendorf, S.A.; Thompson, G. Parameterization of cloud microphysics based on the prediction of bulk ice particle properties. Part II: Case study comparisons with observations and other schemes. *J. Atmos. Sci.* **2015**, *72*, 312–339. [CrossRef]
55. Hsu, N.; Jeong, M.J.; Bettenhausen, C.; Sayer, A.; Hansell, R.; Seftor, C.; Huang, J.; Tsay, S.C. Enhanced Deep Blue aerosol retrieval algorithm: The second generation. *J. Geophys. Res. Atmos.* **2013**, *118*, 9296–9315. [CrossRef]
56. Kaufman, Y.; Tanré, D.; Remer, L.A.; Vermote, E.; Chu, A.; Holben, B. Operational remote sensing of tropospheric aerosol over land from EOS moderate resolution imaging spectroradiometer. *J. Geophys. Res. Atmos.* **1997**, *102*, 17051–17067. [CrossRef]
57. Sayer, A.M.; Hsu, N.C.; Bettenhausen, C.; Holz, R.E.; Lee, J.; Quinn, G.; Veglio, P. Cross-calibration of S-NPP VIIRS moderate-resolution reflective solar bands against MODIS Aqua over dark water scenes. *Atmos. Meas. Tech.* **2017**, *10*, 1425–1444. [CrossRef]
58. Prata, A. Infrared radiative transfer calculations for volcanic ash clouds. *Geophys. Res. Lett.* **1989**, *16*, 1293–1296. [CrossRef]
59. Sayer, A.; Hsu, N.; Lee, J.; Bettenhausen, C.; Kim, W.; Smirnov, A. Satellite Ocean Aerosol Retrieval (SOAR) algorithm extension to S-NPP VIIRS as part of the "Deep Blue" aerosol project. *J. Geophys. Res. Atmos.* **2018**, *123*, 380–400. [CrossRef] [PubMed]